Published by
NIGERIAN SOCIETY OF PHYSICAL SCIENCES
Available online @ https://journal.nsps.org.ng/index.php/jnsps

J. Nig. Soc. Phys. Sci. 8 (2026) 3556

Journal of the Nigerian Society of Physical Sciences

Stratigraphic controls on reservoir quality in the deep-offshore Niger Delta: Integrated sequence-stratigraphic and petrophysical evidence from the 'BX' Field

A. O. Fajana *, O. I. Aduloju

Department of Geophysics, Federal University Oye-Ekiti, Nigeria

Abstract

Reservoir development in the Niger Delta is affected by geological uncertainties arising from complex stratigraphic architecture, high-frequency sea-level changes, fault-controlled subsidence, and variable sediment supply, which complicate prediction of reservoir geometry, continuity, and quality. This study integrates sequence stratigraphy and petrophysical analysis of the deep-offshore "BX" Field, Niger Delta Basin, to define stratigraphic controls on reservoir distribution and quantify properties relevant to hydrocarbon potential and field development. Three-dimensional seismic data and well-log suites from four wells were integrated to interpret sequence boundaries and maximum flooding surfaces and establish Lowstand, Transgressive, and Highstand System Tracts. The interpreted surfaces were correlated with seismic reflectors and diagnostic well-log patterns to constrain facies distribution, sandstone-body geometry, and reservoir architecture. Across interpreted hydrocarbon-bearing intervals, effective porosity ranges from 21.4% to 29.0%, permeability from 3.00 D to 21.49 D, net-to-gross ratio from 0.67 to 0.96, and hydrocarbon saturation from 57.96% to 77.07%. The water-dominated BX-R0 interval in well BX-04, with hydrocarbon saturation of 17.69%, was excluded from hydrocarbon-pay comparisons but retained in reservoir-rock-quality comparisons. Reservoir quality is generally most favourable within Lowstand and selected Highstand System Tracts, whereas Transgressive System Tracts contain more shale and show lower reservoir efficiency. Integrated sequence-stratigraphic and petrophysical evaluation therefore provides a useful basis for reservoir-heterogeneity prediction, reservoir modelling, and development planning in complex deep-water depositional systems of the Niger Delta Basin.

DOI: 10.46481/jnsps.2026.3556

Keywords: Reservoir, Offshore, Sequence boundaries, Petrophysical evaluation, Reservoir heterogeneity

Article History:
Received: 29 May 2026
Received in revised form: 10 July 2026
Accepted for publication: 14 September 2026
Available online: 24 September 2026

Communicated by: B. J. Falaye

1. Introduction

1.1. Background of the study

One of the most enduring problems of deep-offshore petroleum systems, especially in areas of post-depositional complexity, structural deformation, and sparse well control, is reservoir-quality prediction according to Ref. [1]. In this type of setting, the question is not just one of the presence of sandstone reservoirs, but whether the sands are laterally continuous, sufficiently clean, well-connected, and able to produce commercial hydrocarbons according to Refs. [2, 3]. This is particularly true in high-cost deep-water settings, where the accuracy of reservoir prediction may have an important impact on field appraisal, development planning, and recovery strategy. The Niger Delta Basin is one of the most productive hydro-

*Corresponding Author Tel. No.: +234-803-825-9701.
Email address: akindeji.fajana@fuoye.edu.ng (A. O. Fajana)

carbon provinces in Sub-Saharan Africa. The petroleum system is contained in a thick sedimentary wedge that developed through multiple cycles of marine transgression and regression driven by both eustatic sea-level fluctuations and tectonic activity according to Refs. [4, 5]. This has resulted in a highly heterogeneous stratigraphic framework and reservoirs that are often compartmentalized according to Refs. [6, 7], with laterally variable petrophysical properties, shale intercalations, and complex sandstone geometry and lithofacies according to Refs. [8, 9].

Good reservoir description in the Niger Delta therefore cannot be achieved simply by identifying sand-bearing intervals on well logs according to Ref. [10]. It requires an understanding of how depositional processes and stratigraphic architecture control sandstone distribution, reservoir connectivity, and fluid-storage capacity according to Refs. [11, 12].

This challenge can be addressed using sequence stratigraphy, which relates depositional patterns of stratigraphic units to changes in accommodation, sediment supply, and relative sea level according to Refs. [13, 14]. The identified stratigraphic surfaces (sequence boundaries and maximum flooding surfaces) can be used to organize reservoir intervals into genetically related depositional units, such as Lowstand, Transgressive, and Highstand System Tracts according to Ref. [11]. This framework is especially applicable in deep-offshore environments, where reservoir sands may occur in basin-floor fans, slope-channel complexes, incised-valley fills, shoreface deposits, or other depositional elements with widely variable geometries and qualities. Well-log data, when combined with seismic data, allow sequence stratigraphy to predict the presence, distribution, and possible field-wide connectivity of reservoir sands.

This stratigraphic framework is supplemented by petrophysical analysis, which provides a quantitative assessment of reservoir performance. Parameters such as porosity, water saturation, permeability, shale volume, hydrocarbon saturation, and net-to-gross ratio are critical for evaluating storage capacity, flow potential, and reservoir effectiveness according to Ref. [15]. These properties are most meaningful, however, within their depositional and stratigraphic context. Even a high-quality sandstone may perform poorly if it is not laterally persistent, is shaly, is compartmentalized, or is poorly interconnected with other reservoir units according to Refs. [7, 9, 11]. Similarly, the same petrophysical values may have different development implications in lowstand, transgressive, or highstand depositional settings. Studies of the Niger Delta have shown that some of the most favourable reservoir facies occur within Lowstand System Tracts, where high-energy depositional processes may form well-sorted, clean sandstones such as incised-valley fills, slope fans, or basin-floor fan deposits according to Refs. [14, 16]. By contrast, Transgressive System Tracts are generally characterized by increased marine flooding, greater shale content, and reduced reservoir effectiveness. Highstand deposits may also form good reservoirs where sediment supply is sufficient and depositional energy remains favourable.

These observations indicate that petrophysical properties are not the only factors controlling reservoir quality; rather, reservoir quality results from the interaction of sediment supply, depositional energy, stratigraphic position, facies architecture, and post-depositional modification. Although sequence-stratigraphic and petrophysical techniques have been increasingly adopted in Niger Delta reservoir studies, their integration at field scale remains incomplete and is particularly challenging in the deep offshore, where reservoir architecture is often difficult to determine. Many studies emphasize stratigraphic interpretation without adequately quantifying reservoir properties, whereas others emphasize petrophysical evaluation without fully explaining depositional controls on reservoir variability. This leaves a knowledge gap regarding the interaction among system tracts, facies distribution, and petrophysical heterogeneity and their control on reservoir quality and hydrocarbon distribution at field scale. The deep-offshore 'BX' Field in the western Niger Delta provides a suitable setting for addressing this problem. The field is a complex hydrocarbon system in both stratigraphic and structural terms, and reservoir-rock quality varies among depositional units and system tracts.

This study aims to improve understanding of reservoir distribution, facies architecture, and controls on reservoir characterization through integrated sequence-stratigraphic and petrophysical assessments. Integrating seismic interpretation, well-log correlation, stratigraphic-surface mapping, and quantitative petrophysical evaluation provides a more coherent basis for predicting reservoir heterogeneity and identifying intervals with better hydrocarbon potential. This approach clarifies the influence of stratigraphic architecture and petrophysical properties on reservoir quality in the deep-offshore Niger Delta. Reservoir prediction in the BX Field therefore depends not only on recognizing sand-rich intervals but also on their stratigraphic position and depositional processes. This integrated approach provides a stronger basis for reservoir modelling, development planning, and optimization of hydrocarbon recovery in complex deep-water depositional systems.

1.2. Location of the study area

The study was carried out on the 'BX' Field, located in the deep-offshore Niger Delta Basin, approximately 120 km offshore the coast of southern Nigeria and within the 500 m seabed water-depth contour (500 m isobath) (Figure 1). The 3-D seismic survey covers approximately 251 km^2, with the field extending from approximately 499,200 to 508,000 mE and 556,800 to 561,600 mN, referenced to the Minna datum, Nigeria West Belt / UTM Zone 31N (EPSG:26391) (Figure 2).

2. Geology of the study area

The Niger Delta occupies a coastal and offshore sector of the Gulf of Guinea and broadly corresponds to the Niger Delta Province as delineated according to Ref. [21]. Cartographic representations of the province commonly show the maximum petroleum-system boundary, principal structural limits, and the minimum extent of the petroleum system as inferred from mapped oil- and gas-field centres according to Ref. [17]. These

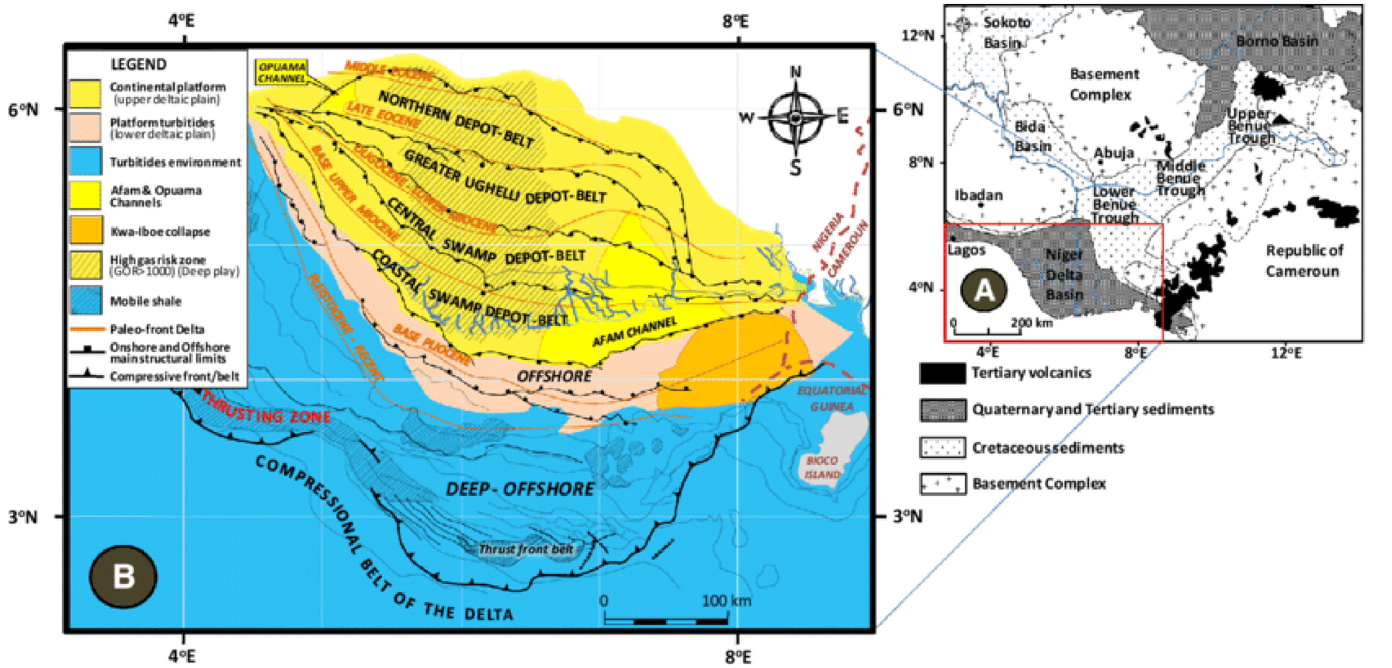

Figure 1: Geologic map of Nigeria showing the location of the Niger Delta Basin and sectional map of the Niger Delta depobelts and structural limits according to Refs. [17, 18].

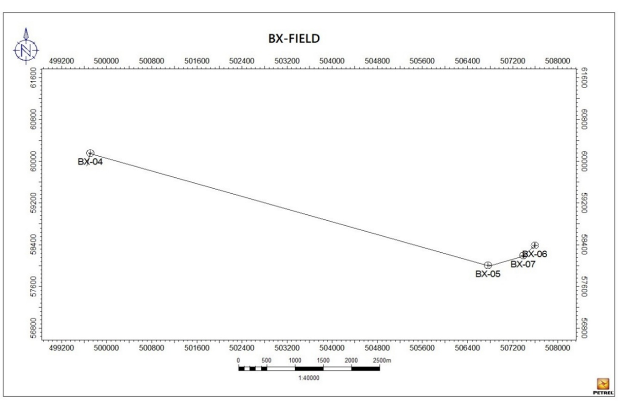

Figure 2: Map showing wells in the "BX" Field aligned along northwest–southeast (NW–SE) and southeast (SE) trends.

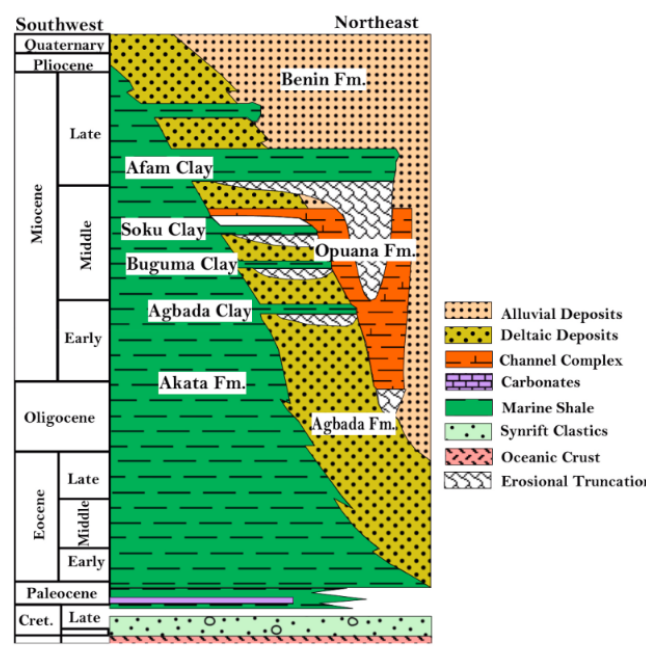

Figure 3: Stratigraphic cross-section of the Niger Delta Basin (SW–NE) showing the transition from deep-marine (Akata Formation) to deltaic (Agbada Formation) and alluvial deposits (Benin Formation,) with key depositional features and structural elements. Adapted from Refs. [19, 20].

maps also typically depict bathymetric contours and sediment-thickness patterns, generally on the order of 2–4 km. Over geological time, the basin developed a single dominant Tertiary petroleum system commonly referred to as the Akata–Agbada system, which defines the main hydrocarbon endowment of the province according to Ref. [22].

The system's broadest geographic limit aligns with the provincial boundary, while its minimum mapped extent is constrained by the areal distribution of discovered fields. Stratigraphically, the delta has prograded broadly southwestward since at least the Eocene, forming a series of depositional belts (depobelts) that record the locus of the most active sedimentation at successive time intervals according to Ref. [18]. Each depobelt results from the interplay between sediment supply and accommodation space controlled by subsidence; when sedimentation outpaces local accommodation, the depocentre migrates basinward and a new depobelt forms. The depobelts

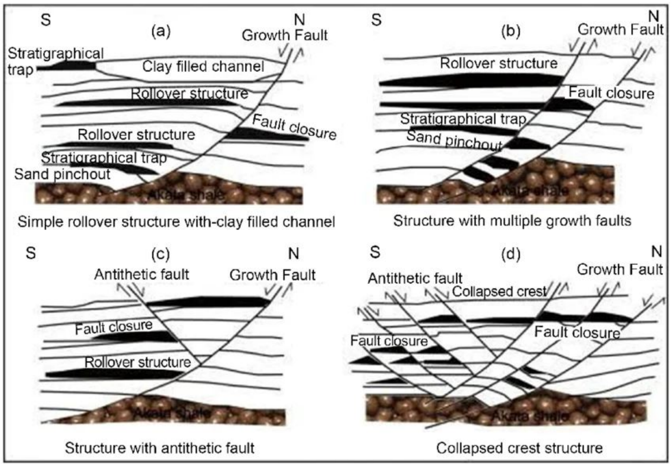

Figure 4: Common structures and traps delineated in oil fields in the Niger Delta according to Ref. [21].

are usually separated by regional growth faults and other syndepositional structural features. The oldest recognized sedimentary unit overlying the crystalline basement in the Niger Delta is the Cretaceous succession. Although no boreholes have penetrated this sequence beneath the Niger Delta Basin itself, the basin represents the southernmost and geologically youngest extension of the Benue–Abakaliki Trough according to Refs. [17, 23]. Its lithology has been inferred from exposures in the adjacent Anambra Basin to the northeast. The Niger Delta geology is characterized by sand–shale alternations, and these reservoirs are classified as deltaic sandstones according to Ref. [24].

The Eocene Agbada Formation lies directly above the Akata Formation and is the principal hydrocarbon-bearing unit. Reservoir depths in the Niger Delta, including the "BX" Field, range from 5,000 to 14,000 ft, demonstrating the substantial vertical extent of productive intervals. This stratigraphic and depositional context highlights the geological suitability of the area for hydrocarbon exploration and production according to Refs. [23, 24].

The Niger Delta's stratigraphic evolution (Figure 3) occurred through five southwestward-prograding depobelts bounded by syndepositional fault systems and formed through the interaction of sediment supply and subsidence (Figure 4). The petroleum system is mostly derived from marine shales in the Agbada and deeper Akata Formations; research indicates that the Agbada shales primarily generate oil, whereas the Akata shales primarily generate gas according to Refs. [17, 22].

In the field, structural traps include faults and anticlines. These are typical of the Niger Delta, which is known to contain dip-closure, stratigraphic, and fault-bounded traps (Figure 4). Growth faults and antithetic faults are important to trap configuration. Growth faults may extend for several tens of kilometres, are arcuate and concave basinward, and may have throws of up to several hundred metres. The throw of an antithetic fault is usually less than 100 m. In plan view, antithetic faults may be linear or arcuate and seldom exceed 10 km in length.

2.1. Materials used for the study

The materials used for this study include a base map of the study area, which covers approximately 62,023 acres (approximately 251 km^2). The map shows the seismic grid, comprising inlines and crosslines along which the seismic data were acquired, and the locations of the four wells: BX-04, BX-05, BX-07, and BX-06. Lithological discrimination and reservoir delineation were carried out using the available well-log data, including gamma-ray (GR), resistivity (ILD), density (RHOB), neutron-porosity (NPHI), and sonic logs. To align seismic data in time with well data in depth, checkshot data, which measure travel times from surface shotpoints to geophones at known well depths, were used for time-to-depth conversion. These data were combined with sonic and density logs to improve depth conversion, create synthetic seismograms, and enable well-to-seismic ties. Checkshot data were available only for BX-04 and were used to establish the time–depth relationship for that well. For the remaining wells, depth conversion and well-to-seismic ties were based on the available sonic and density logs and the established velocity relationship, with the associated depth and tie uncertainties considered.

A post-stack 3-D full-stack seismic volume was used as the principal structural and stratigraphic interpretation volume. A separate near-stack product supplied with the dataset was used specifically for seismic-to-well tying. The full-stack volume enables visualization of the subsurface through two-dimensional sections (inlines and crosslines) and time slices, providing the structural and stratigraphic framework. The dataset comprises a post-stack 3-D seismic volume containing approximately 670 inlines and 420 crosslines, with inline numbers ranging from 6649 to 7321 and crossline numbers from 925 to 1349 (Figure 5). The survey employed a line spacing of 20 m, and the data were provided in SEG-Y format. The polarity follows the American standard, with peaks represented by blue and troughs by red. The seismic volume exhibits reflection geometries ranging from strong, continuous events to weaker, more discontinuous reflections. Table 1 summarizes the data available for this study.

2.2. Methods used for the study

The methodology began with collection of data stored in standard digital formats and loading the datasets into Petrel™ for processing. After loading, a comprehensive quality-control (QC) procedure was performed to ensure data integrity and reliability before interpretation. The first stage of petrophysical analysis involved qualitative interpretation of the relationships and patterns of the gamma-ray, resistivity, density, neutron, and sonic logs in Petrel. Lithology was interpreted primarily from the gamma-ray (GR) log (Figure 6), calibrated over a 0–150 American Petroleum Institute (API) range. The observed minimum gamma-ray value of 5.70 API was used as GRmin (the clean-sand endpoint), while 150 API was used as GRmax (the shale endpoint) for gamma-ray normalization. The normalized gamma-ray index was then used in the Larionov equation to estimate shale volume. A cut-off interval of 70–80 API was selected from the observed separation between low-GR, sand-dominated intervals (< 70 API) and high-GR, shale-dominated

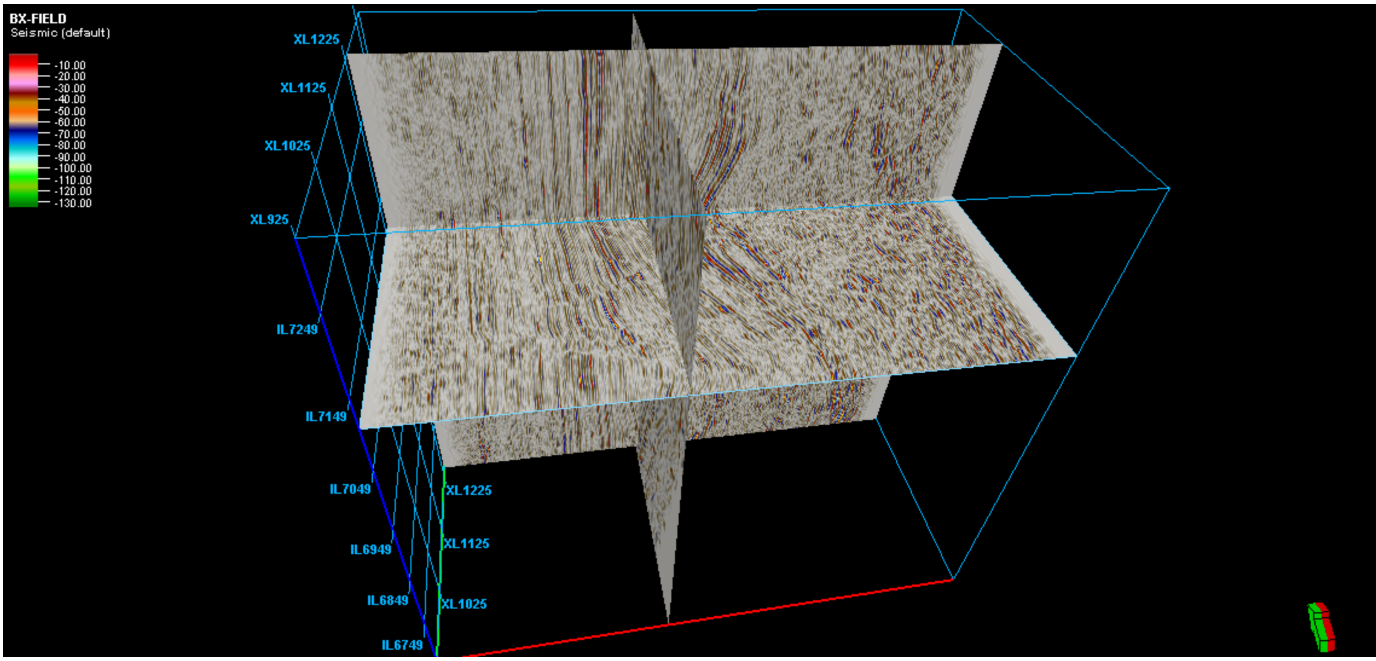

Figure 5: 3-D full-stack seismic volume of the “BX” Field showing typical inline 7110, crossline XL 1240, and time slice Z (-2500).

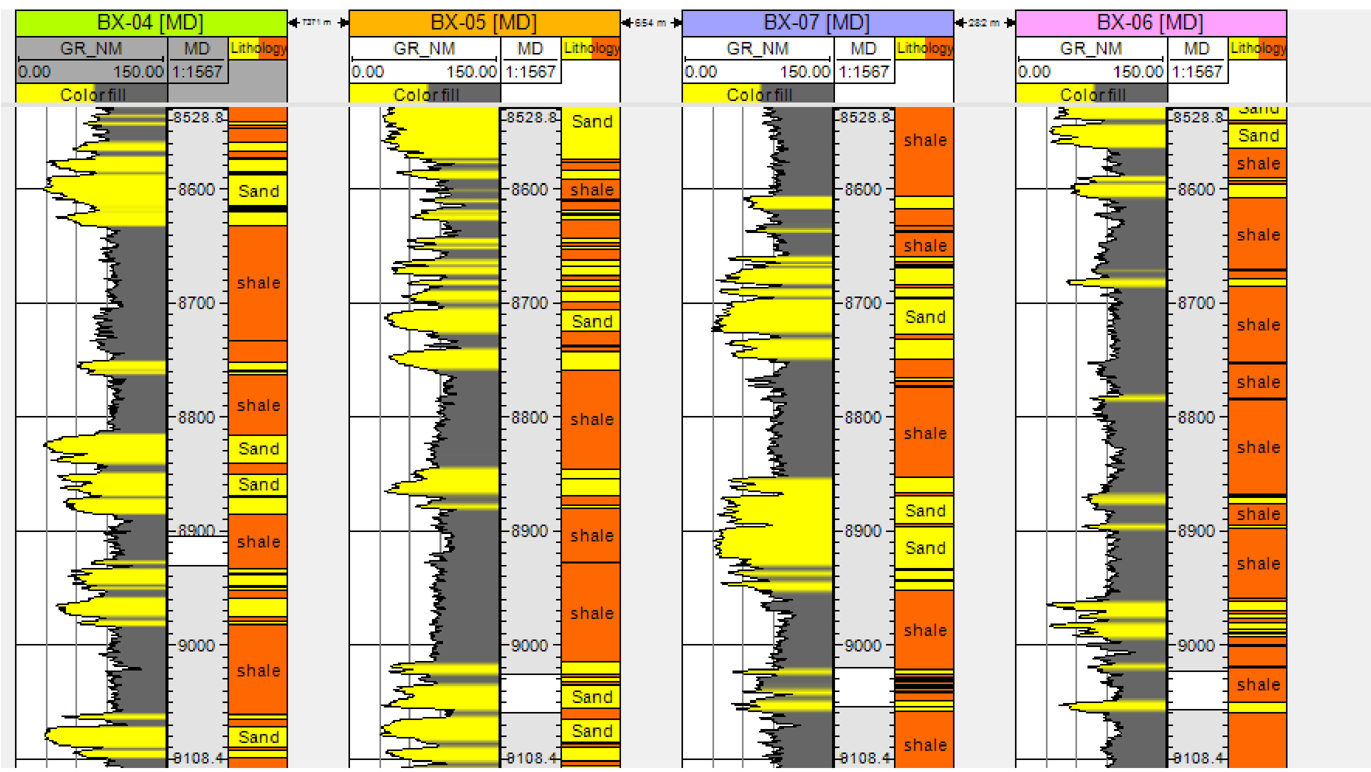

Figure 6: Lithology delineation across all wells in the BX Field using the gamma-ray log.

intervals (> 80 API), while 70–80 API represents transitional shaly-sand responses. For net-sand determination, GR < 70 API was treated as sand-prone, 70–80 API as transitional shaly sand, and GR >80 API as shale-prone. The 70–80 API transitional interval was excluded from clean net-sand thickness in the primary net-to-gross calculation.

The reservoirs were identified through analysis of the gamma-ray and deep-resistivity logs. Hydrocarbon-bearing zones show low gamma-ray and high resistivity values. Where responses were ambiguous, density and neutron logs were used for additional verification of fluid type and to reduce uncertainty. Fluid contacts were identified by integrating the density,

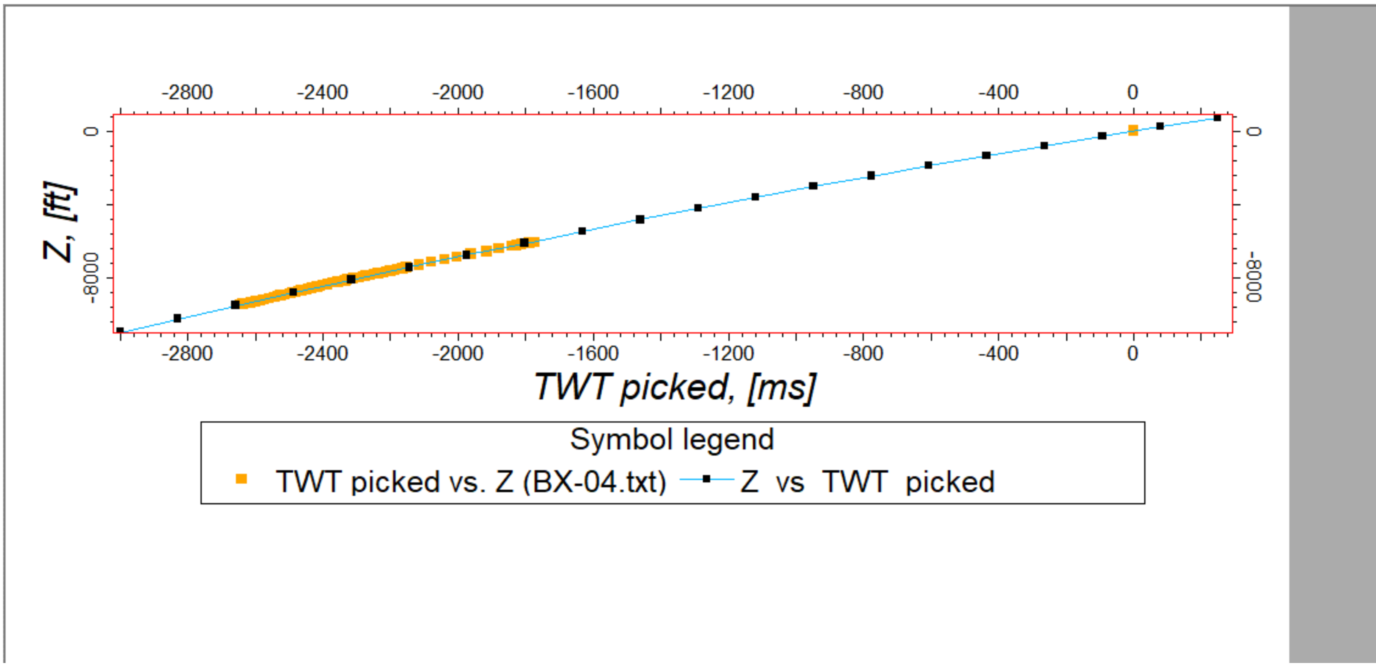

Figure 7: Polynomial function for well BX-04 used to convert the time map to a structural depth map in the BX Field.

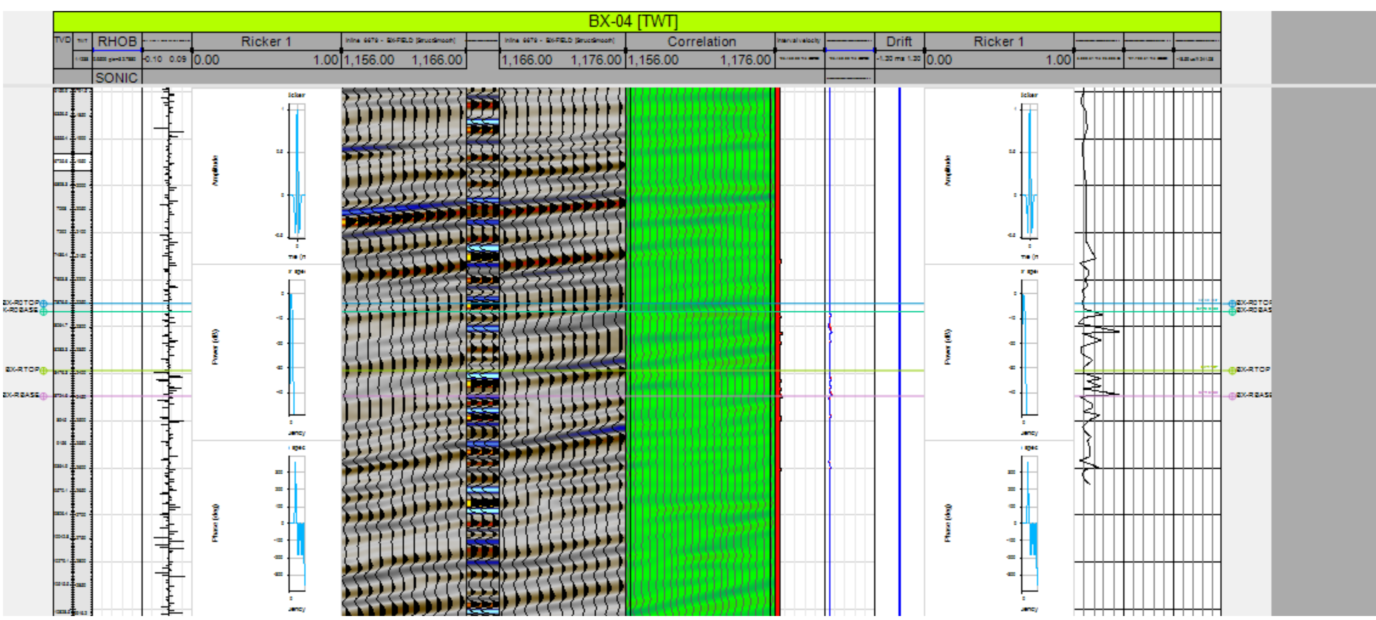

Figure 8: Seismic-to-well tie generated from well BX-04 in the BX Field.

Table 1: Summary of the available well data.

Well	Checkshot	Deviation data	GR	RES	RHOB	NPHI	SONIC
BX-04	Available	Available	Available	Available	Available	Available	Available
BX-05	Unavailable	Available	Available	Available	Available	Available	Available
BX-07	Unavailable	Available	Available	Available	Available	Available	Available
BX-06	Unavailable	Available	Available	Available	Available	Available	Available

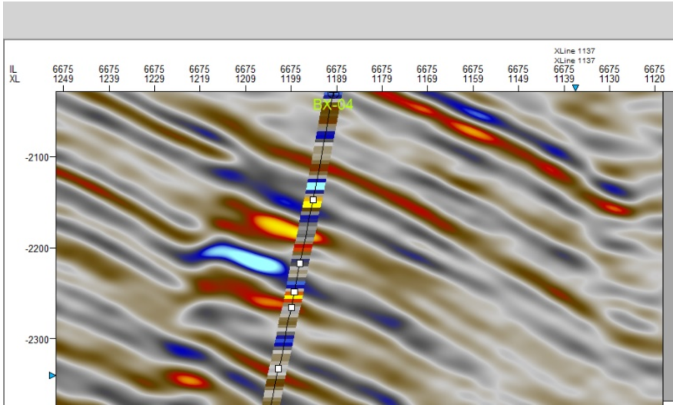

Figure 9: Synthetic seismogram tie between well data and seismic data in the BX Field.

neutron, and resistivity logs. Neutron–density crossover was used as a supporting indicator of changes in fluid and lithological conditions. Fluid contacts, particularly the oil–water contact, were interpreted primarily from changes in resistivity response, with pressure, capillary-pressure, or formation-test data considered where available. Where direct fluid-contact evidence was unavailable, the interpreted contact was treated as uncertain and constrained using the available well-log and structural information.

Well correlation was based on integration of well-log signatures, sequence-stratigraphic surfaces, and 3-D seismic interpretation. Laterally continuous shale intervals identified from the gamma-ray and resistivity logs were used as correlation markers where continuity was supported by seismic reflection character and their relationship to interpreted sequence boundaries and maximum flooding surfaces. The identified sequence-stratigraphic surfaces provided the primary framework for establishing stratigraphic equivalence between wells, while shale intervals served as supporting markers. Where log or seismic continuity was ambiguous, the correlation was treated as uncertain and alternative interpretations were considered.

2.3. *Quantitative log interpretation*

2.3.1. *Gross thickness*

Gross reservoir thickness represents the full stratigraphic interval that includes both sand and shale. It was determined by measuring the depth difference between the reservoir top and base according to Ref. [25]:

$$\text{Gross Thickness} = \text{Base of Reservoir} - \text{Top of Reservoir}. \quad (1)$$

2.3.2. *Net thickness*

Net-sand thickness is the interval comprising sand only within a reservoir. It was determined by subtracting shale-interval thickness from gross thickness:

$$\text{Net thickness} = \text{Gross thickness} - \text{Shale interval thickness}. \quad (2)$$

2.3.3. *Net-to-gross thickness*

Net-to-gross ratio is the ratio of net thickness to gross reservoir thickness:

$$\text{NTG} = \frac{\text{Net thickness}}{\text{Gross thickness}}. \quad (3)$$

2.3.4. *Volume of shale*

Shale volume is a measure of the quantity of shale present in the reservoir rock. It was calculated from the gamma-ray log. The gamma-ray index was computed as:

$$I_{\text{GR}} = \frac{GR_{\text{log}} - GR_{\text{min}}}{GR_{\text{max}} - GR_{\text{min}}}, \quad (4)$$

where IGR is the gamma-ray index, GRlog is the gamma-ray response across the reservoir interval, GRmax is the gamma-ray response of shale, and GRmin is the minimum gamma-ray response of clean sand. The age of the rock affects the computed shale volume.

Consequently, the equation of Ref. [26] was used for the final shale-volume computation:

$$V_{\text{sh}} = 0.083\left(2^{3.7 I_{\text{GR}}} - 1.0\right). \quad (5)$$

2.3.5. *Porosity*

Porosity was calculated from the bulk-density log using the density-porosity equation:

$$\phi_D = \frac{\rho_{\text{ma}} - \rho_b}{\rho_{\text{ma}} - \rho_f}, \quad (6)$$

where ϕ_D is density-derived porosity, ρ_b is the bulk density of the formation, ρ_{ma} is matrix density, and ρ_f is fluid density.

A matrix density of 2.65 g/cm^3 was used for the sandstone matrix. Fluid density was assigned according to the interpreted pore-fluid type using the values adopted in the study. The basis and assumed pressure, temperature, and salinity conditions for the selected fluid densities are stated where available. The calculated density porosity was subsequently corrected for shale volume to obtain effective porosity. Uncertainty in the assumed matrix and fluid densities is recognized as a potential source of uncertainty in the calculated porosity.

Effective porosity was subsequently determined by accounting for shale content. Effective porosity represents the interconnected pore space considered available for hydrocarbon storage and flow. The shale correction was implemented in Petrel using:

$$\phi_e = \phi_D - (V_{\text{sh}} \times \phi_{\text{sh}}), \quad (7)$$

where ϕ_{sh} is the density-derived porosity of the local shale end-point.

The resulting total and effective porosity values were used in the subsequent petrophysical evaluation, with effective porosity used in the permeability estimation. Because core-porosity measurements were unavailable, these values are treated as log-derived estimates rather than core-calibrated measurements.

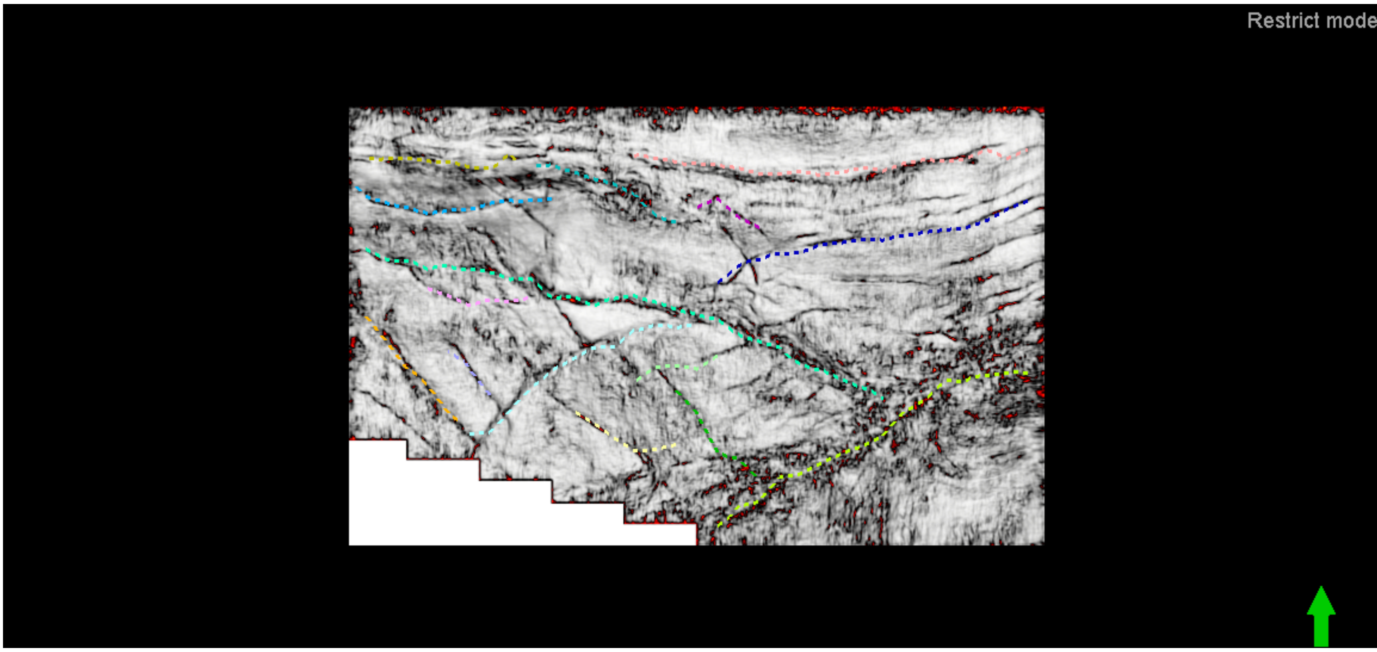

Figure 10: Time-variance attribute used to aid fault mapping in the BX Field.

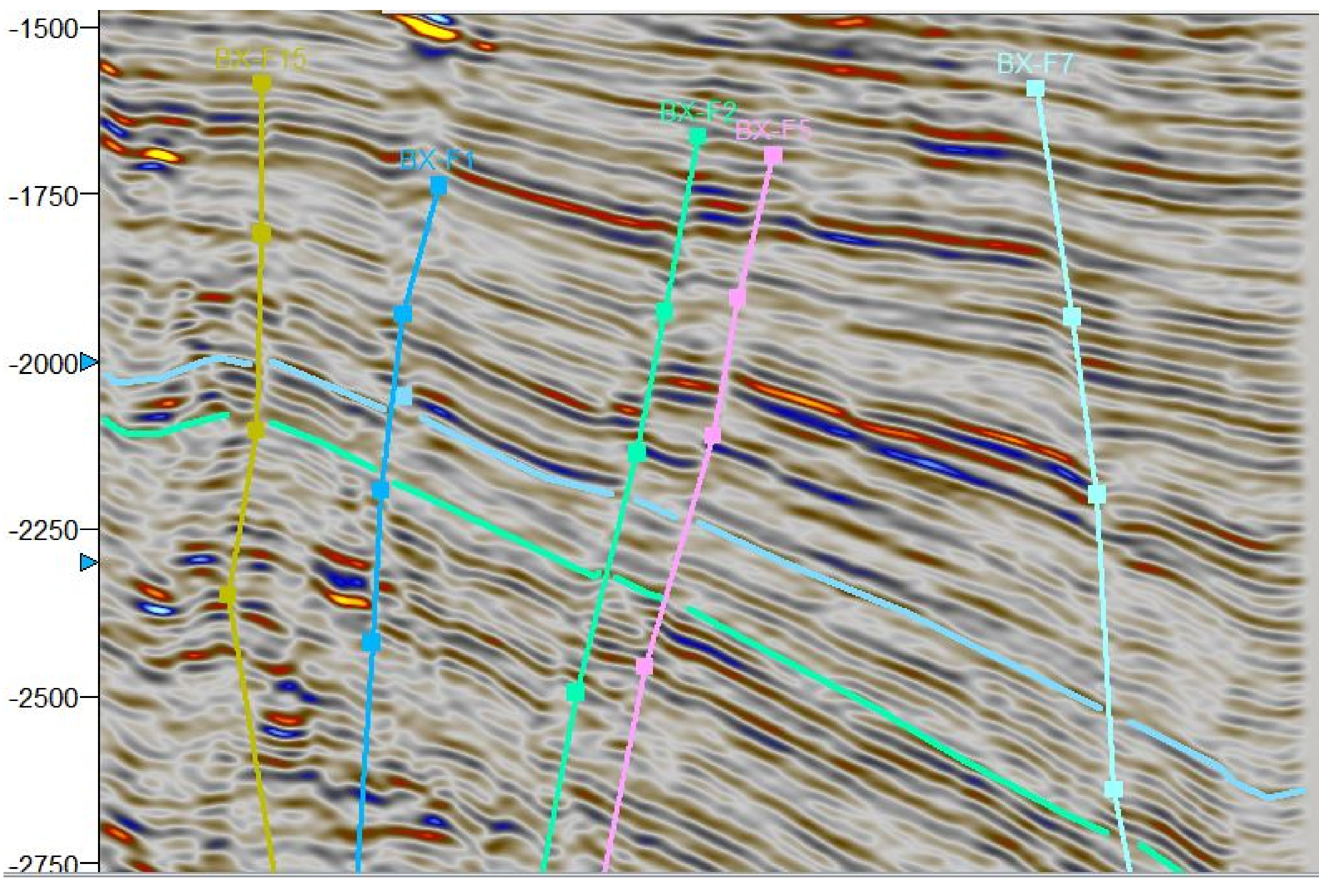

Figure 11: Faults and horizons mapped in the BX Field.

2.4. *Permeability (K)*

The Wyllie–Rose-type empirical correlation was selected to estimate permeability because it relates permeability to porosity and irreducible water saturation (Swirr), which are parameters available from the well-log interpretation according to Ref. [24]. Because no core-permeability measurements were

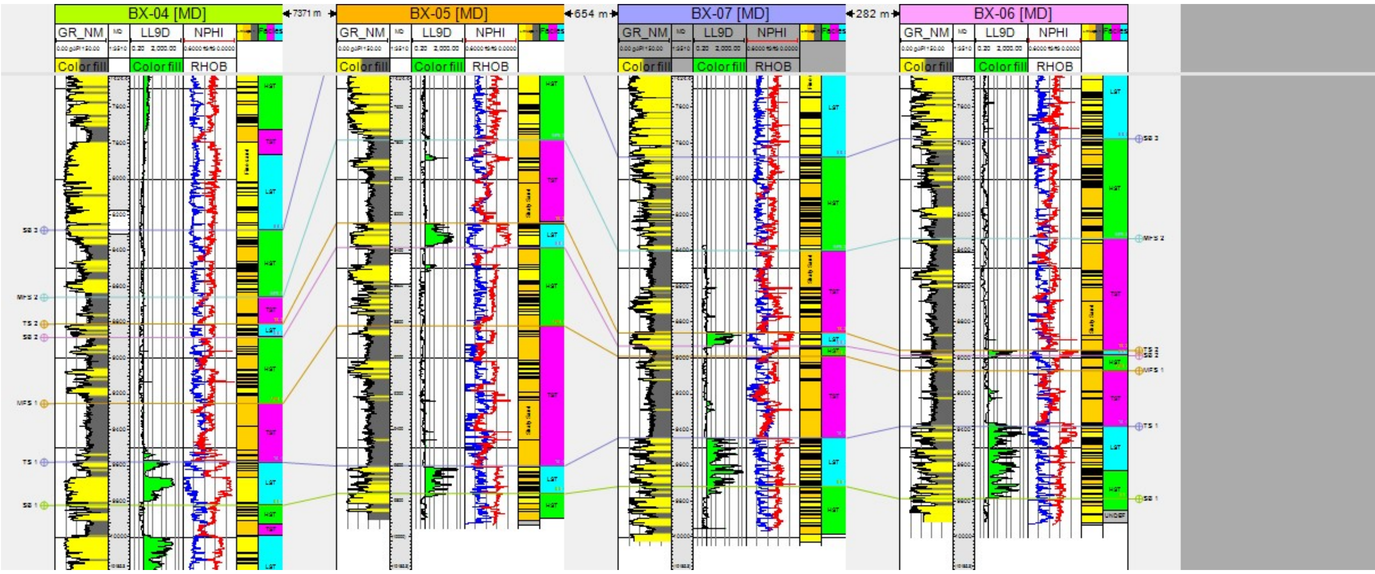

Figure 12: Sequence-stratigraphic correlation across BX-04, BX-05, BX-07, and BX-06.

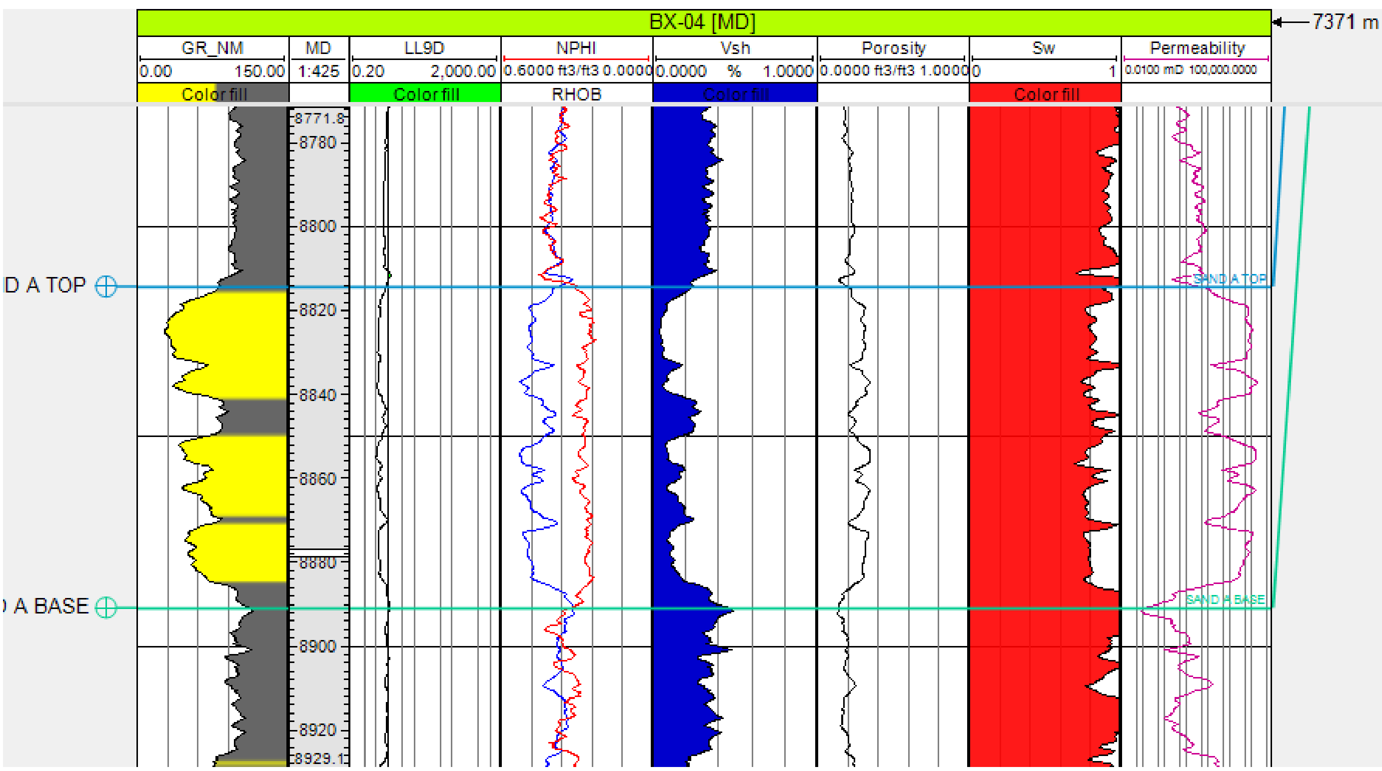

Figure 13: Logs of analyzed petrophysical properties for reservoir BX-R0 in well BX-04.

available, the resulting permeability values are treated as empirical log-derived estimates.

$$K(\mathrm{mD}) = \left(\frac{250 \times \Phi^3}{S_{\mathrm{wirr}}} \right)^2, \tag{8}$$

where K is permeability in millidarcies, Φ is effective porosity, and S_{wirr} is irreducible water saturation.

The conversion from millidarcies to darcies is given by:

$$K(\mathrm{D}) = \frac{K(\mathrm{mD})}{1000}. \tag{9}$$

2.4.1. Water saturation (Sw)

Archie's equation according to Ref. [27] provides the basis for estimating water saturation in clean formations where shale conductivity is negligible:

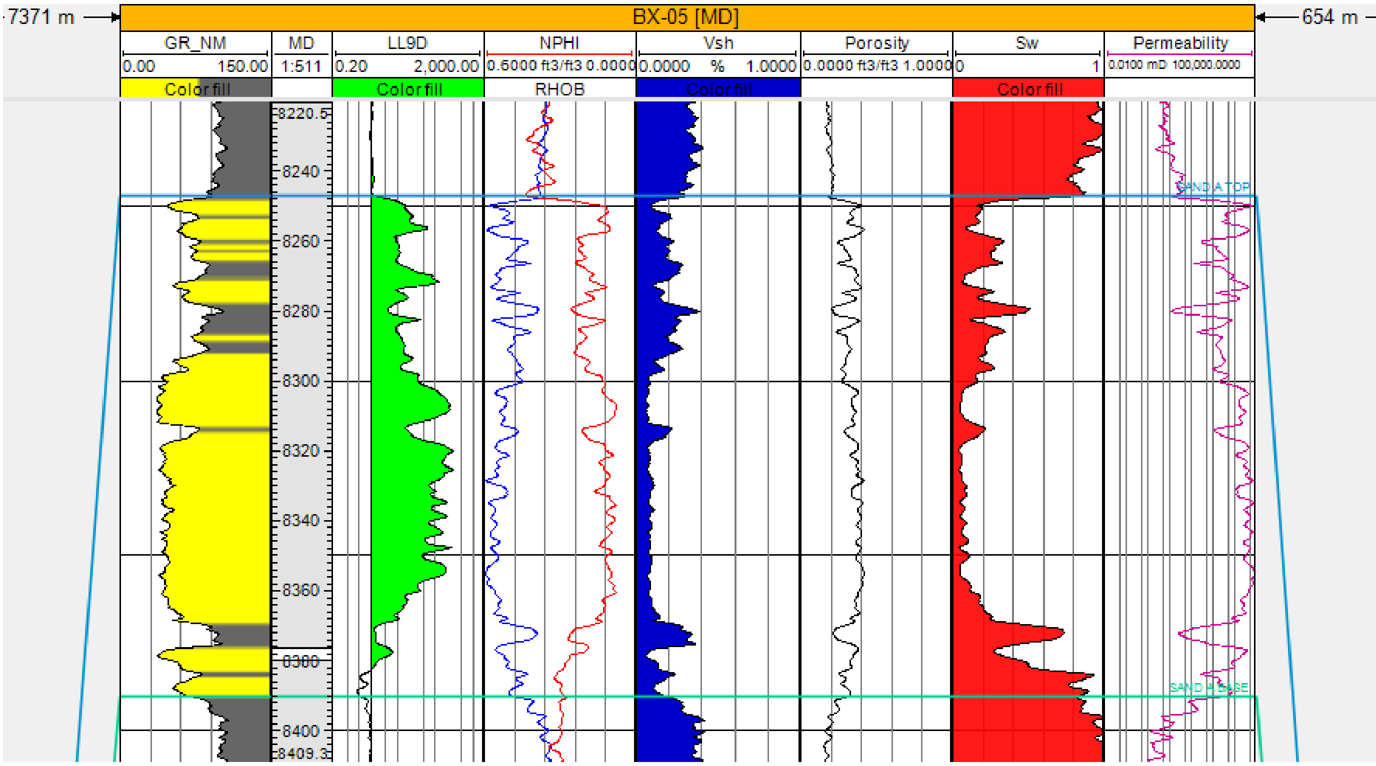

Figure 14: Logs of analyzed petrophysical properties for reservoir BX-R0 in well BX-05.

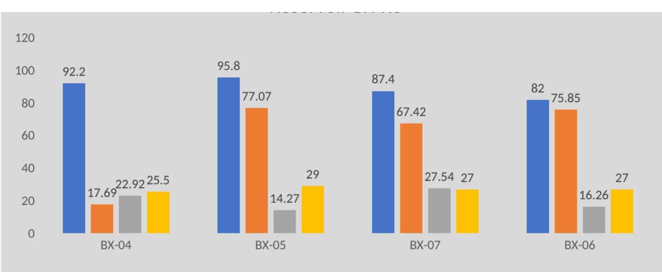

Figure 15: Statistical representation of average computed petrophysical parameters for reservoir BX-R0 in the four wells.

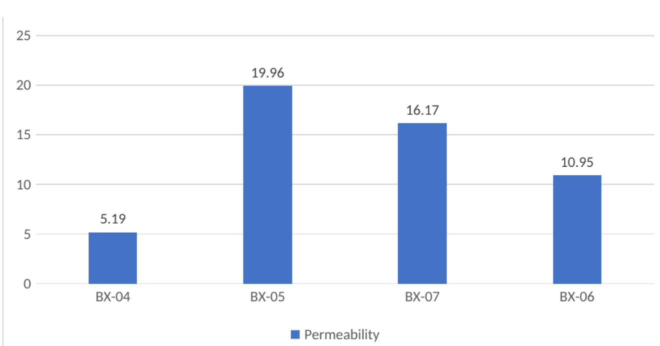

Figure 16: Statistical representation of average computed permeability for reservoir BX-R0 in the four wells.

$$S_w^n = \frac{a \times R_w}{R_t \times \Phi_t^m}. \tag{10}$$

For this study, water saturation (Sw) was calculated using the Modified Simandoux model, which accounts for the conductive effect of shale on formation resistivity according to Refs. [28, 29]. The equation is given as:

$$\frac{1}{R_t} = \frac{S_w^2}{F \times R_w(1 - V_{\text{sh}})} + \frac{V_{\text{sh}} \times S_w}{R_{\text{sh}}}, \tag{11}$$

where S_w is water saturation, R_t is true formation resistivity (Ω·m), R_w is formation-water resistivity (Ω·m), R_{sh} is shale resistivity (Ω·m), V_{sh} is shale volume (fraction), ϕ_t is total porosity (fraction), a is the tortuosity factor, m is the cementation exponent, and n is the saturation exponent. For the sandstone intervals, a = 0.62, m = 2.15, and n = 2.0 were adopted consistently. Rw was calibrated from the cleanest water-dominated interval in BX-R0 at BX-04, while Rsh was taken from adjacent thick shale intervals on the deep-resistivity log. In the absence of laboratory formation-water and core electrical-property measurements, the resulting Sw values are treated as model-dependent estimates.

2.4.2. Irreducible water saturation

Irreducible water saturation was estimated from formation factor using an approximate log-based relationship according to Ref. [29]:

$$S_{\text{wirr}} = \sqrt{\frac{F}{2000}}, \tag{12}$$

where F is the formation factor.

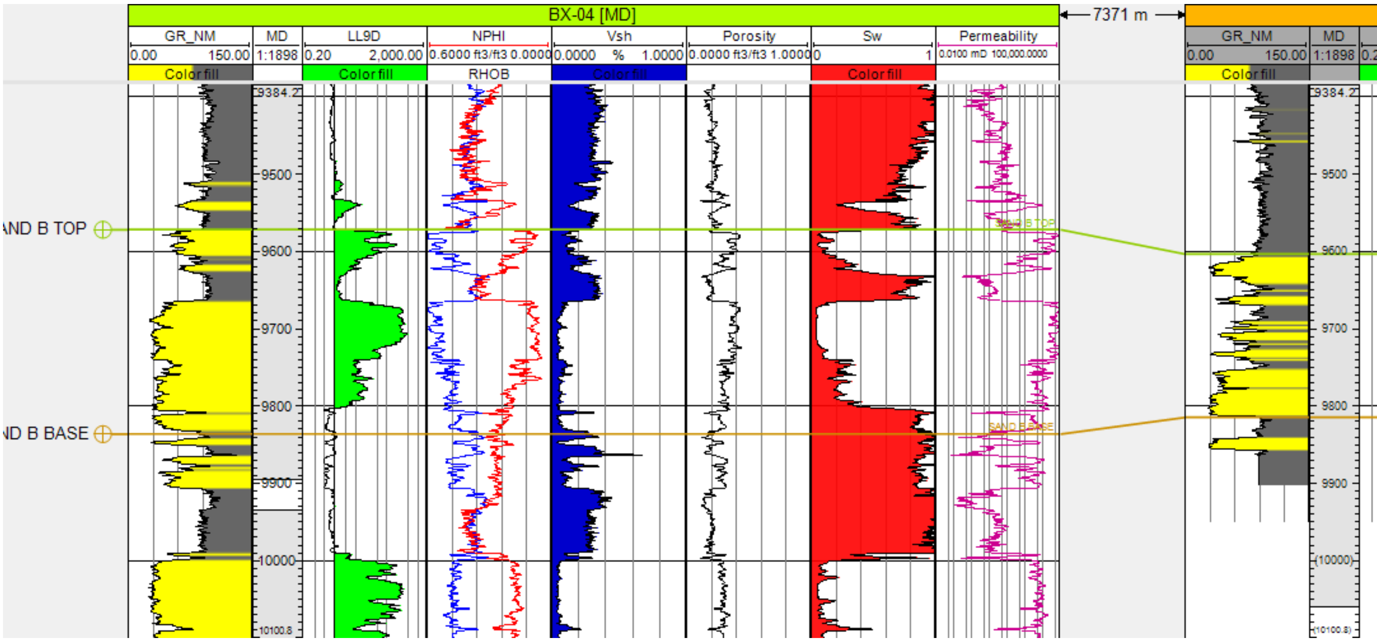

Figure 17: Logs of analyzed petrophysical properties for reservoir BX-R in well BX-04.

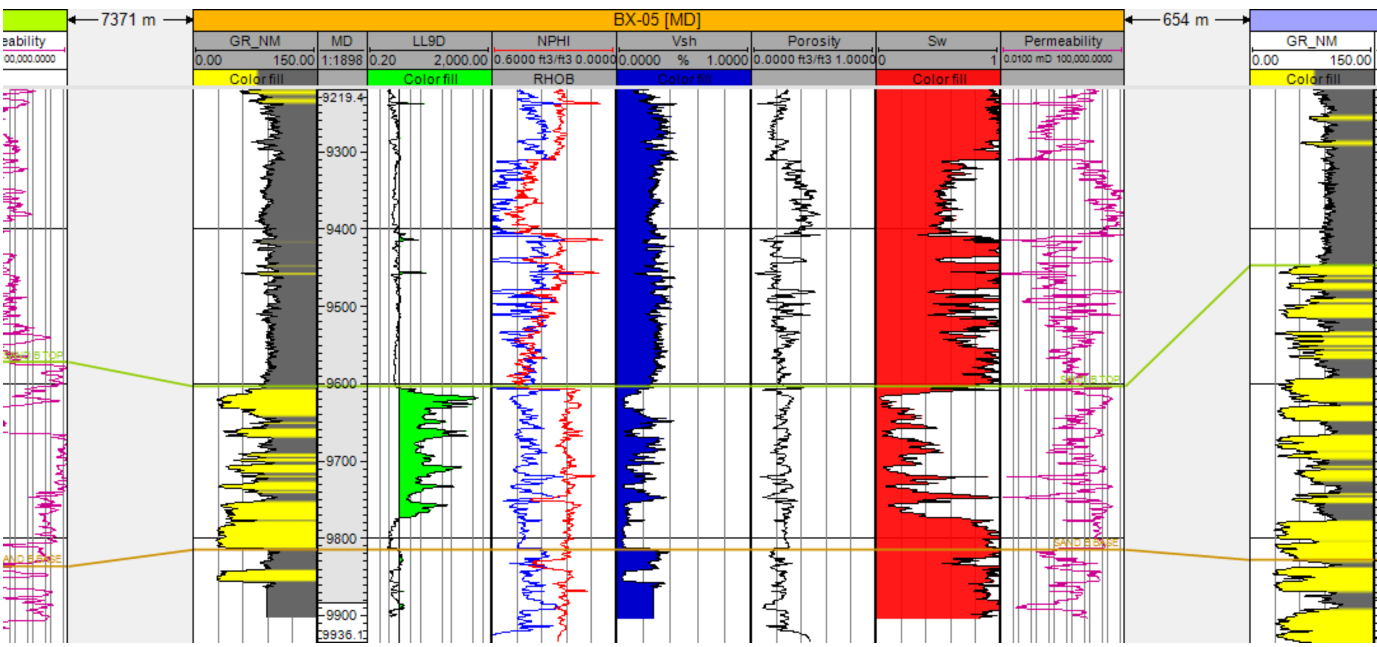

Figure 18: Logs of analyzed petrophysical properties for reservoir BX-R in well BX-05.

The formation factor was calculated using Archie's relationship according to Ref. [27]:

$$F = \frac{R_0}{R_w}, \tag{13}$$

where R_0 is the resistivity of the formation when 100% water saturated, and R_w is formation-water resistivity. Where R_0 was not directly available, the equivalent Archie form $F = a/\phi^m$ was used with the same a and m values adopted in the saturation model.

2.4.3. *Hydrocarbon saturation (S_h)*

Hydrocarbon saturation is the fraction of pore space in a reservoir rock that is occupied by hydrocarbons (oil and/or gas) rather than formation water.

It is expressed as:

$$S_h = 1 - S_w, \tag{14}$$

where S_h is hydrocarbon saturation, S_w is water saturation, and 1 represents 100% of the pore volume.

As a percentage, hydrocarbon saturation is expressed as:

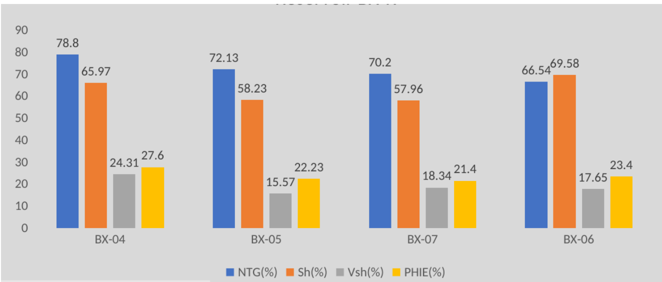

Figure 19: Statistical representation of average computed petrophysical parameters for reservoir BX-R in the four wells.

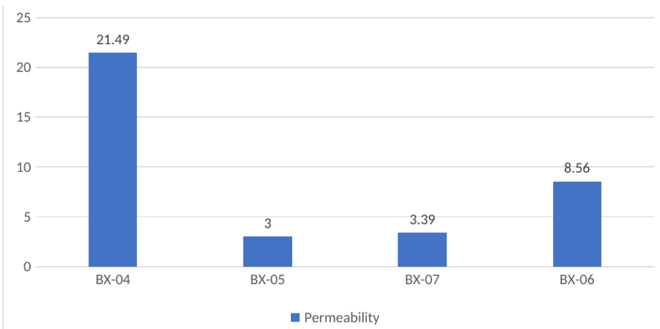

Figure 20: Statistical representation of average computed permeability for reservoir BX-R in the four wells.

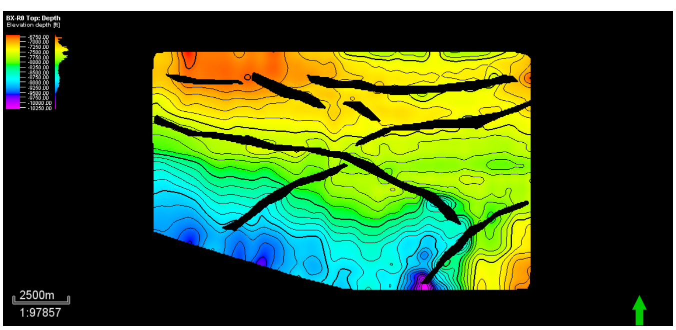

Figure 21: Depth map for the top of reservoir BX-R0.

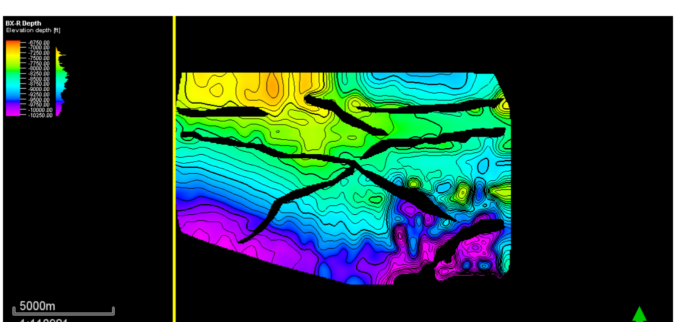

Figure 22: Depth map for the top of reservoir BX-R.

$$S_h(\%) = (1 - S_w) \times 100. \quad (15)$$

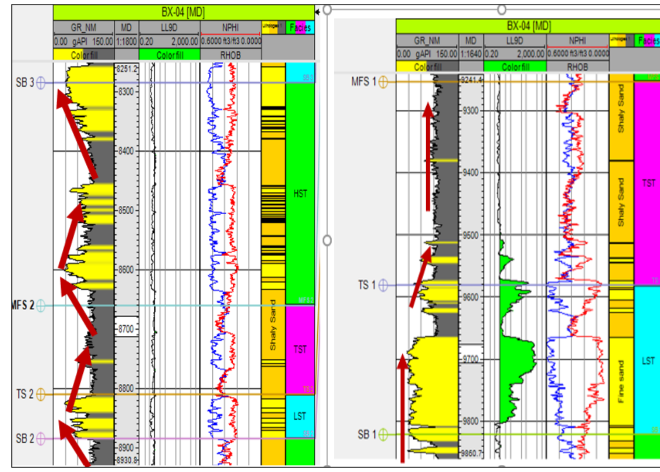

Figure 23: Identification of transgressive surfaces (TS), maximum flooding surfaces (MFS), sequence boundaries (SB), and system tracts (LST, TST, HST) in BX-04.

2.5. *3-D seismic interpretation*

The study utilized a post-stack 3-D seismic dataset for structural and stratigraphic interpretation. The full-stack seismic volume served as the primary interpretation volume and was used for fault and horizon mapping. Seismic sections were examined along inlines and crosslines, while time slices and arbitrary lines were generated where necessary to improve the identification of structural and stratigraphic features.

2.5.1. *Seismic-to-well tie*

Seismic-to-well tying was performed to establish the relationship between well-log-derived synthetic seismic responses and the seismic data and to improve confidence in horizon identification. Figure 7 shows the time-to-depth conversion curve for well BX-04. The separate near-stack seismic product was used for the well tie (Figure 8) because it represents the near-zero-offset response and provided the most appropriate seismic response for comparison with the synthetic seismogram. A Ricker wavelet, with the interpretation-project setting recorded as 40/20 Hz, was used for convolution, and a bulk shift of -10 ms was applied to obtain the best visual alignment between the synthetic and seismic responses (Figure 9).

2.5.2. *Fault mapping*

Faults were mapped perpendicular to the fault-dip direction on both crosslines and inlines at an interval spacing of 20 × 20 inline/crossline for this study. The full-stack seismic data volume was used for fault interpretation, while the variance attribute was used to enhance fault mapping (Figure 10).

2.5.3. *Horizon mapping*

Horizons are time-equivalent seismic surfaces corresponding to laterally continuous depositional/stratigraphic events. After the well-to-seismic tie and fault interpretation, horizon mapping was performed. The tied wells provided control points

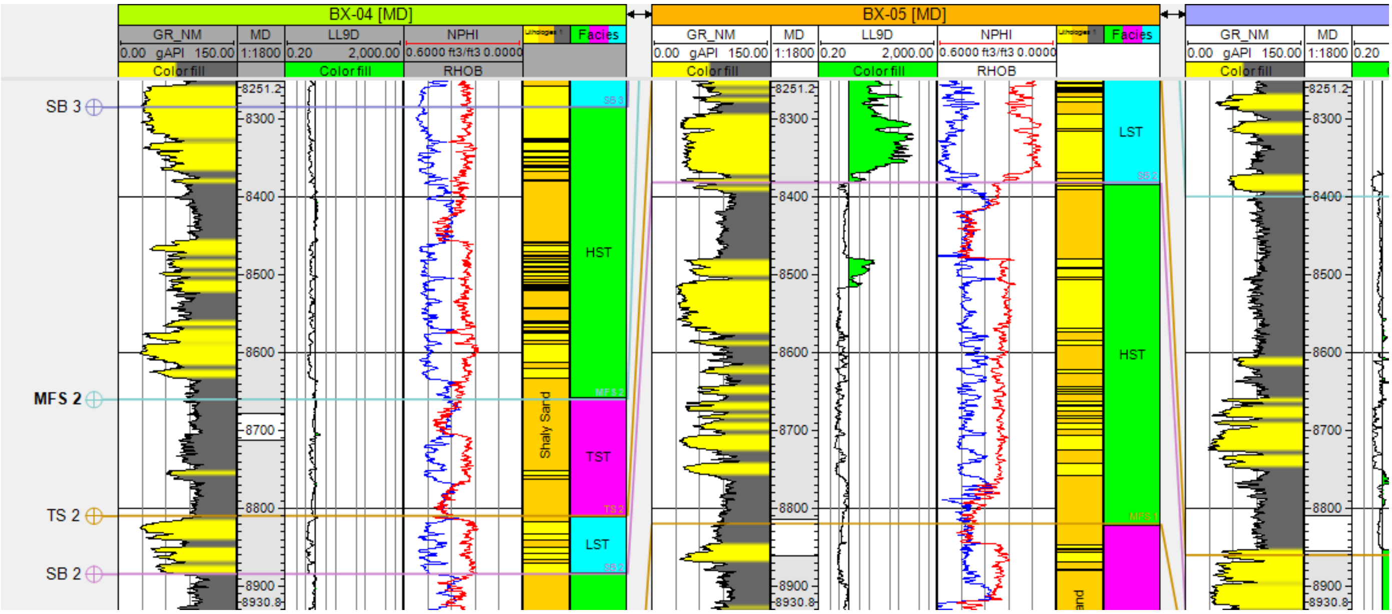

Figure 24: Identification of transgressive surfaces (TS), maximum flooding surfaces (MFS), sequence boundaries (SB), and system tracts in BX-05, BX-07, and BX-06.

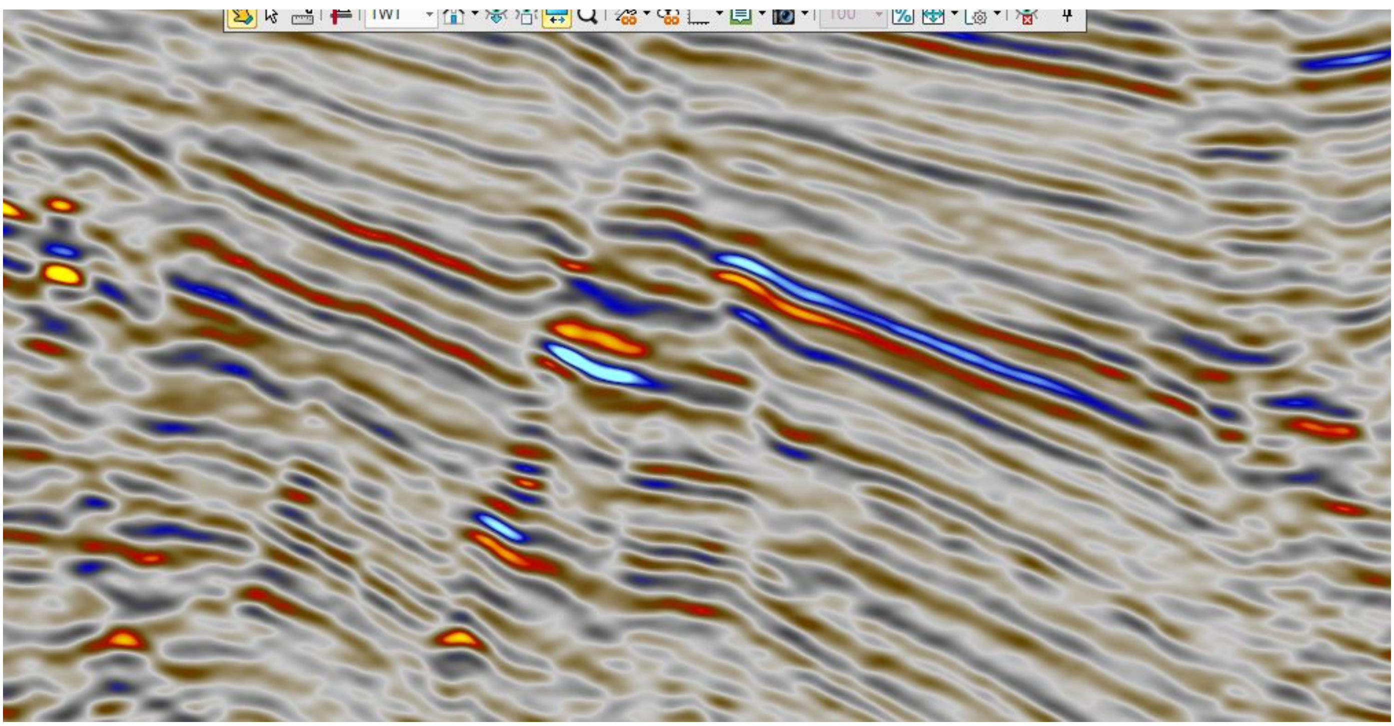

Figure 25: Sequence-stratigraphic correlation on the seismic section.

for selecting and tracking key reflectors throughout the seismic volume. The identified horizons were then extrapolated laterally from these well-tie points, and gridded time surfaces were created from the 3-D seismic data. These interpreted horizons and mapped faults were then used in Petrel to create time-surface maps and define the structural setting of the reservoir intervals, as illustrated in Figures 10 and 11.

2.5.4. Structural modelling

Three-dimensional seismic horizons, faults, and fault polygons were interpreted and mapped for structural modelling. Seismic interpretation was performed in the time domain, after which the interpreted time-structure maps were converted to depth by applying the calibrated velocity model described below. This conversion was required because reservoir geometry, structural closure, and volumetric parameters are better under-

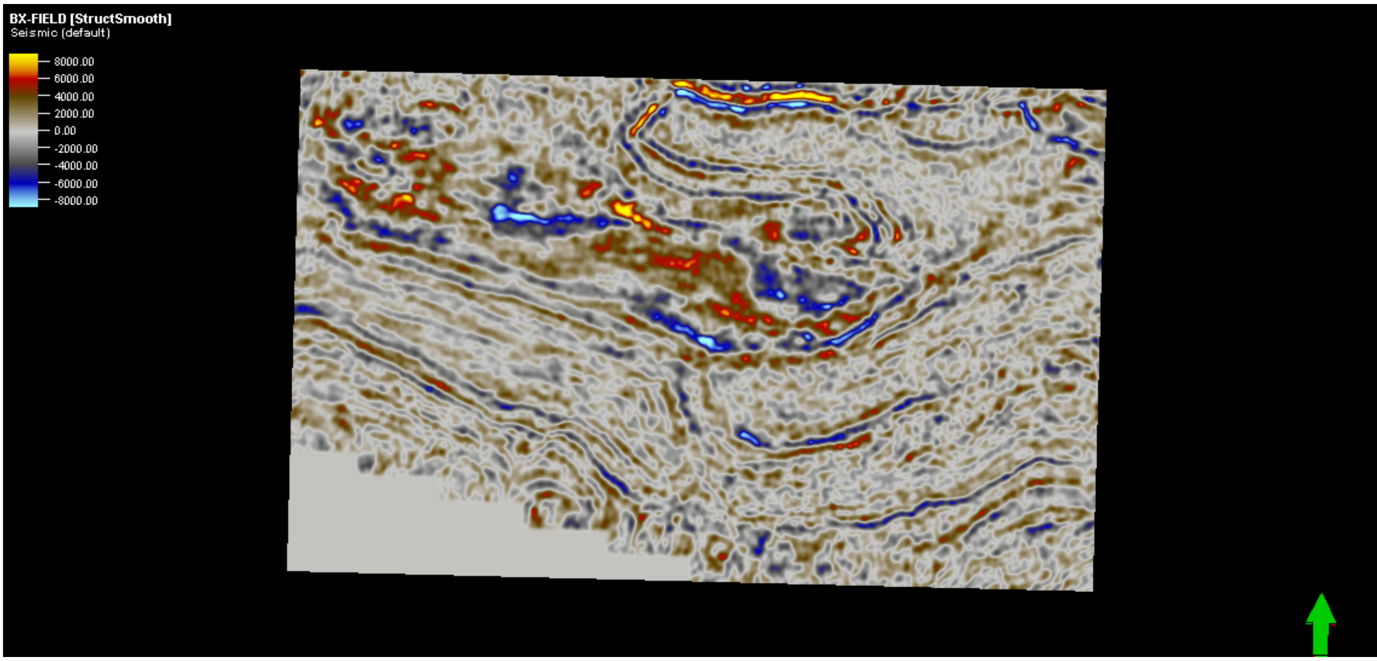

Figure 26: Vertical subsurface structural-attribute section through the BX Field around the 3000 ms two-way-time interval.

stood in the depth domain than in the seismic-time domain according to Ref. [27]. Depth conversion used the relationship between two-way travel time (TWT) and average seismic velocity:

$$Z = Z_{\text{datum}} + \frac{V_{\text{avg}} \times TWT}{2}, \tag{16}$$

where Z is the depth to the target horizon, Z_{datum} is the reference datum, V_{avg} is the average velocity, and TWT is the two-way travel time. The average velocity was derived from well control using:

$$V_{\text{avg}} = \frac{2(Z - Z_{\text{datum}})}{TWT}. \tag{17}$$

The available time-depth data were fitted to a polynomial velocity function and used to create a continuous velocity model. The generalized polynomial function is given as:

$$V_{\text{avg}} = a_0 + a_1 T^1 + a_2 T^2 + \cdots + a_n T^n, \tag{18}$$

where a_0 to a_n are polynomial coefficients, T is travel time, and n is the polynomial order. The generated velocity model was then applied to the interpreted time-structure maps to obtain depth-structure maps of the reservoir horizons. Because the calibration is based principally on BX-04, the polynomial model is treated as a field-scale approximation rather than a fully constrained multiwell velocity model.

The horizons, fault polygons, and fault traces that were interpreted were the main input data used for the generation of depth surfaces. Fault polygons were added to account for the discontinuities across the fault planes and to avoid an unrealistic surface interpolation across the structurally separated compartments. The depth-converted surfaces were then compared to the depths of well tops and the regional structural trends to ensure consistency between the seismic interpretation, well control, and the final structural framework. Reservoir geometry, structural closures and fault-bound compartments were defined within the study area using the final structural model. The depth-converted surfaces were checked against available well tops, but the absence of independent checkshot control in BX-05, BX-07, and BX-06 prevents a rigorous quantitative depth-uncertainty envelope from being established.

2.6. Sequence-stratigraphic inferences

Sequence stratigraphic interpretation was done using a combination of the wireline-log response and seismic reflection characteristics. Key stratigraphic surfaces, depositional packages, systems tracts, and depositional environments were identified for the studied interval. Well-log and seismic data were also integrated; lithological changes seen in the wells were then correlated to the depositional geometry and stratal architecture seen in the seismic data.

Vertical lithofacies trends and depositional stacking patterns were interpreted largely from gamma-ray log motifs. Funnel-shaped patterns were interpreted as upward-coarsening successions, typically related to progradational depositional packages. Bell-shaped motifs were interpreted as upward-fining successions, which are often associated with channel-fill or transgressive deposits. Cylindrical motifs were interpreted as relatively uniform sand-prone bodies, and serrated motifs as heterolithic or interbedded sand–shale intervals. Where available, these log-based interpretations were calibrated against resistivity and porosity-log responses.

Seismic facies, reflector continuity, amplitude character, reflector terminations, and stratigraphic position were used to constrain the final depositional-environment interpretation because gamma-ray motifs are not uniquely diagnostic of depositional environment according to Ref.[30]. Depositional geometries were identified using seismic reflection patterns, including progradation, aggradation, retrogradation, onlap, downlap, and truncation. This integration provided a stronger basis for linking seismic character, sedimentary interpretation, and reservoir properties. Log character and seismic-reflection configuration were used to interpret key sequence-stratigraphic surfaces. Sequence boundaries were recognized from abrupt vertical facies changes, sharp sand bases, erosional truncation, and/or down-dip facies shifts into the basin. Shale-rich intervals, high gamma-ray responses, laterally persistent seismic reflectors, and downlap relationships were used to identify maximum flooding surfaces. Transgressive surfaces were interpreted at the onset of retrogradational stacking patterns where deposition changed from relatively sand-prone to shale-prone.

The interpreted surfaces were used to subdivide the succession into systems tracts. Sand-prone deposits overlying sequence boundaries were used to identify lowstand systems tracts (LST). Retrogradational stacking patterns and increasing shale content characterized transgressive systems tracts (TST). Aggradational to progradational stacking patterns above maximum flooding surfaces were interpreted as highstand systems tracts (HST). The resulting sequence-stratigraphic framework was used to support depositional-environment interpretation and explain the vertical and lateral distribution of reservoir and non-reservoir facies.

The sequence-stratigraphic correlation across BX-04, BX-05, BX-07, and BX-06 (Figure 12) shows a succession of sequence boundaries (SB), transgressive surfaces (TS), and maximum flooding surfaces (MFS). SB1, TS1, MFS1, SB2, TS2, MFS2, and SB3 correlate across the wells, defining two complete depositional sequences, SB1–SB2 and SB2–SB3, together with partial intervals outside the bounding surfaces where present.

The resulting sequence-stratigraphic framework was used to support depositional-environment interpretation and explain the vertical and lateral distribution of reservoir and non-reservoir facies according to Ref. [31].

The surfaces correlate laterally, but the thickness and vertical development of the LST, TST, and HST differ from well to well. This reflects how accommodation, sediment supply, and depositional architecture changed across the field.

3. Results and discussion

3.1. Well correlation

Well-log interpretation revealed three lithological units: sand, sandy shale, and shale. Well-log correlation from northwest to southeast showed two reservoir intervals that can be stratigraphically correlated across the four wells (BX-04, BX-05, BX-07, and BX-06). These reservoirs were designated BX-R0 and BX-R. This stratigraphic correlation does not by itself demonstrate hydraulic connectivity between wells or across fault-bounded compartments.

3.1.1. Petrophysical analysis of reservoir BX-R0

Results of the petrophysical analyses of reservoirs BX-R0 and BX-R are shown in Tables 2 and 3. Reservoir BX-R0 in wells BX-04, BX-05, BX-07, and BX-06 has gross thicknesses of 76.54 ft, 143.09 ft, 103.16 ft, and 33.28 ft, respectively. In BX-04 (Figure 13), the interval was interpreted as water-dominated with minimal hydrocarbon presence. Its low gamma-ray values indicate sand-prone lithology, whereas the low resistivity response and hydrocarbon saturation of 17.69% indicate water dominance. The interval was therefore excluded from hydrocarbon-pay comparisons but retained in reservoir-rock-quality comparisons. In BX-05 (Figure 14), BX-R0 exhibits favourable static reservoir and hydrocarbon-saturation characteristics, with a gross thickness of 143.09 ft, net thickness of 137.09 ft, and net-to-gross ratio of 95.8%. It has the highest porosity, 33.83%, together with low water saturation (22.93%), hydrocarbon saturation of 77.07%, and permeability of 19.96 D.

In BX-07, reservoir BX-R0 has 90.16 ft of net sand and a net-to-gross ratio of 87.4%; its average porosity is 30.79% and average hydrocarbon saturation is 67.42%. However, the average shale volume is higher, at 27.54%, potentially affecting effective porosity. Average permeability is 16.17 D. In BX-06, BX-R0 is thin but displays favourable static reservoir properties. Its 27.28 ft net thickness has an average porosity of 32.08% and average hydrocarbon saturation of 75.85%. The empirical permeability estimate of 10.95 D indicates comparatively favourable static flow potential but does not by itself establish production performance. The average computed petrophysical parameters and permeability values for BX-R0 in the four wells are shown in Figures 15 and 16.

3.1.2. Qualitative and quantitative interpretation of reservoir BX-R in the four wells

Reservoir BX-R in wells BX-04, BX-05, BX-07, and BX-06 is interpreted as hydrocarbon-bearing because the sand lithology corresponds to high resistivity-log values. Gross thicknesses are 330.3 ft, 220.73 ft, 393.02 ft, and 453.98 ft, respectively. Detailed petrophysical analysis was performed across the reservoir in all wells. In BX-04 (Figure 17), BX-R has a gross thickness of 330.3 ft, net thickness of 260.3 ft, and net-to-gross ratio of 78.8%. Average porosity is 31.24%, hydrocarbon saturation is 65.97%, and average permeability is 21.49 D. These parameters indicate favourable static storage and log-derived flow potential but do not by themselves establish primary-production performance.

In BX-05 (Figure 18), BX-R has a net thickness of 159.23 ft and gross thickness of 220.73 ft, with average porosity of 26.05% and average hydrocarbon saturation of 58.23%. The average permeability of 3.00 D indicates comparatively lower static flow potential than BX-R in BX-04. BX-R in BX-07 has 261.52 ft of net sand and a gross thickness of 393.02 ft, while its average porosity of 25.7% and average hydrocarbon saturation of 57.96% are lower. Its average permeability of 3.39 D nevertheless supports its identification as a reservoir interval of potential appraisal interest within the field-scale reservoir framework.

Table 2: Computed petrophysical parameters for reservoir BX-R0.

Well	Top (ft)	Base (ft)	Gross (ft)	Net (ft)	N/G (%)	Por. (%)	Eff. por. (%)	V_{sh} (%)	S_w (%)	S_h (%)	K (D)
BX-04	8814.37	8890.00	76.54	70.54	92.20	28.87	25.50	22.92	82.31	17.69	5.19
BX-05	8247.00	8390.09	143.09	137.09	95.80	33.83	29.00	14.27	22.93	77.07	19.96
BX-07	8845.99	8949.15	103.16	90.16	87.40	30.79	27.00	27.54	32.58	67.42	16.17
BX-06	8959.13	8992.41	33.28	27.28	82.00	32.08	27.00	16.26	24.15	75.85	10.95

Table 3: Computed petrophysical parameters for reservoir BX-R.

Well	Top (ft)	Base (ft)	Gross (ft)	Net (ft)	N/G (%)	Por. (%)	Eff. por. (%)	V_{sh} (%)	S_w (%)	S_h (%)	K (D)
BX-04	9571.43	9901.73	330.30	260.30	78.80	31.24	27.60	24.31	34.03	65.97	21.49
BX-05	9603.04	9823.77	220.73	159.23	72.13	26.05	22.23	15.57	41.77	58.23	3.00
BX-07	9446.64	9839.66	393.02	261.52	70.20	25.70	21.40	18.34	42.04	57.96	3.39
BX-06	9358.45	9812.43	453.98	318.98	66.54	27.78	23.40	17.65	30.42	69.58	8.56

In BX-06, the BX-R pay zone has a net thickness of 318.98 ft and a net-to-gross ratio of 66.54%. It has an average porosity of 27.78% and average hydrocarbon saturation of 69.58%. Its permeability is 8.56 D; these parameters indicate favourable static reservoir quality, although sustainable flow rates and long-term production viability cannot be established without dynamic pressure or production data. The average computed petrophysical parameters and permeability values for BX-R in the four wells are shown in Figures 19 and 20.

3.2. Structural maps

Horizon interpretation generated a grid from which a time-surface map was produced. The time surface for reservoir BX-R0 was then converted to a depth surface using a polynomial function.

3.2.1. Depth map for BX-R0

The BX-R0 (Figure 21) and BX-R (Figure 22) depth maps show four major faults, while the other mapped faults are minor. Major fault F2 trends northwest–southeast, F3 and F12 trend northeast–southwest, and F10 trends east–west. The major faults divide the field into distinct structural blocks. Elevation ranges from approximately -8300 ft to -8700 ft. Intersecting fault trends in the central part of the maps produce fault-assisted closures that may act as traps, especially where upthrown blocks form tight contour loops along fault lines. The mapped surfaces generally deepen southwestward, while local closed contours adjacent to faults suggest fault-assisted structural closures. Structural relief and fault geometry may therefore influence hydrocarbon trapping and compartmentalization, although the depth maps alone do not demonstrate fault seal or prove that hydrocarbon distribution is controlled principally by fault movement.

3.3. Sequence-stratigraphy analysis

Integration of seismic and well-log datasets facilitated identification of three key sequence boundaries (SB1, SB2, and SB3), which define two complete depositional sequences (SB1–SB2 and SB2–SB3). Sequence boundaries were identified from erosional surfaces supported by seismic and well-log stacking patterns. Systems tracts were differentiated from stacking patterns, lithological trends, and position relative to the sequence boundaries (SB) and maximum flooding surfaces (MFS), with ambiguous intervals retained as uncertain.

3.3.1. Depositional-sequence interpretation using logs

The BX-04 well (Figure 23) reveals two complete depositional sequences bounded by sequence boundaries SB1, SB2, and SB3, each with distinctive stacking patterns indicating shifts in sedimentation and sea-level change. The lower sequence begins at SB1 near 9822 ft with a Lowstand System Tract (LST) showing a progradational stacking pattern, expressed as blocky, low-gamma-ray sands that build outward into the basin. Above it, the Transgressive System Tract (TST) shows a retrogradational stacking pattern recognized by upward-fining gamma-ray curves that reflect landward facies migration as sea level rises. The transgressive phase culminates near 8882 ft at maximum flooding surface MFS1, where shale content is highest. A Highstand System Tract (HST) then develops upward toward SB2 with an aggradational-to-progradational, coarsening-upward pattern. The upper complete sequence begins at SB2 and extends upward toward SB3 near 8252 ft, beginning with another progradational LST, followed by a retrogradational TST capped by MFS2. The uppermost HST ends near 8252.5 ft and again exhibits a progradational stacking pattern indicative of renewed basinward sediment buildout during highstand conditions before erosion at SB3. The alternation of progradational, retrogradational, and aggradational stacking patterns reflects cyclic sea-level rise and fall.

Overall, the LST and HST sands in the progradational intervals are likely good reservoir zones, while TST and MFS shales in retrogradational intervals may act as seal layers, defining a complete stratigraphic cycle in BX-04. The BX-05 well log shows two complete depositional sequences between SB1, SB2, and SB3 over the studied interval (Figure 24), marked by the corresponding maximum flooding surfaces

(MFS1–MFS2). The lower complete sequence begins at SB1 at 9858 ft and is characterized by a low gamma-ray (GR) interval (< 70 API), representing a lowstand systems tract (LST). It is followed by a transgressive systems tract (TST) extending upward to 8828 ft and capped by a maximum flooding surface marking peak marine influence, with higher GR readings (> 120 API). The upper complete sequence starts at SB2 at 8380 ft and consists of a Lowstand System Tract that grades upward into a TST and highstand systems tract (HST) before reaching MFS2 at 7781 ft. The upper sequence terminates at SB3, observed at approximately 7158 ft, above a dominant HST with minor shale development. Throughout the log, gamma-ray values fluctuate between 40–150 API, reflecting alternating sandstone and shale intervals. Low-GR zones represent sand-dominated depositional environments that are likely good reservoir intervals, whereas high-GR zones indicate shale-rich transgressive phases. Overall, BX-05 reveals two complete cycles of progradation, retrogradation, and aggradation, indicative of repeated sea-level rise and fall that controlled sediment supply, facies distribution, and reservoir quality in the studied interval.

Similar to BX-04 and BX-05, BX-07 (Figure 24) shows the same field-scale sequence-stratigraphic ordering. The studied succession includes two complete sequences bounded by SB1, SB2, and SB3, together with a partial HST below SB1. A lower coarsening-upward Highstand System Tract (HST) occurs before the first complete sequence at approximately 9718 ft, where the gamma-ray response decreases. Above SB1, the Lowstand System Tract (LST) extends upward toward TS1 and is expressed by a sand-prone interval with channel-fill characteristics; its assignment is based on stratigraphic position together with the log motif rather than gamma-ray shape alone. The overlying Transgressive System Tract (TST), between 9,446 and 8,987 ft, shows upward-increasing GR and greater shale content and is capped by Maximum Flooding Surface MFS1. An upper Highstand System Tract from 8987 to 8931 ft coarsens upward again, indicating renewed progradation before the next bounding surface.

BX-06 (Figure 24) records a very similar but independently readable cycle. The Lowstand System Tract of the lower complete sequence occurs above SB1 and extends toward TS1, with bell-shaped to sand-prone gamma-ray motifs interpreted as channel- or shoreface-fill deposits within the lowstand package. Above it, the TST from 9382 to 8,800 ft is shale-prone, with increasing GR, and is capped by MFS1. An upper HST from 8,800 to 8,252 ft again shows coarsening-upward logs and cleaner sands, marking a regressive progradational phase. In both BX-07 and BX-06, the recurring LST–TST–HST stacking pattern reflects local responses to the same relative sea-level and sediment-supply changes, but the logs show facies thicknesses and sand/shale ratios that are distinct to each well.

3.3.2. Depositional-sequence analysis on seismic

The seismic section (Figure 25) tied to well BX-04 shows the stratigraphic architecture and reflection terminations that define the key sequence-stratigraphic surfaces SB1, TS1, MFS1, MFS2, SB2, and SB3 of the "BX" Field, corresponding closely to the log-defined sequences in the well. The reflectors show clear onlap, downlap, and toplap geometries, which are typical indicators of changing depositional conditions during sea-level rise and fall. In the lower part of the section, the interval from SB1 to TS1 is interpreted as LST from its stratigraphic position and associated sand-prone log character, although local reflectors onlap the sequence boundary. Retrogradational and onlapping geometries become more evident above TS1 within the TST. MFS1 marks maximum marine flooding. Moving upward, the interval between SB2 and MFS2 shows parallel and continuous reflectors, while the interval from MFS2 to SB3 represents the HST portion of the upper complete sequence and is capped by truncation or erosion at SB3 related to relative sea-level fall. Onlap at SB1 is therefore not used alone to classify the SB1–TS1 interval as transgressive; the systems-tract interpretation is based on the combined surface hierarchy, log-stacking pattern, and seismic geometry.

Parallel and gently dipping reflections above MFS1 and MFS2 are consistent with highstand deposition.

3.4. Seismic-attribute analysis

Figure 26 displays a vertical subsurface structural-attribute section around the 3000 ms two-way-time interval that explains features observed on the BX-R0 and BX-R depth maps. The image reveals major faults and folds as discontinuous red and blue bands corresponding to the same northeast–southwest- and northwest–southeast-trending faults mapped on both depth maps. The central part of the seismic section displays warped, gently dipping reflectors forming a synclinal structure, while deeper zones show more chaotic and tightly folded reflectors consistent with the deeper depressions on the BX-R map. Strong red–blue reflections occur locally near the crest; however, amplitude alone is not treated as a direct indicator of sandstone or hydrocarbon because it may also reflect impedance contrast, tuning, and processing effects. Downward thickening and increased reflector curvature toward the base match the fault-bounded troughs in the BX-R horizon.

3.5. Reservoir heterogeneity and structural controls on hydrocarbon distribution

Reservoir properties in the BX Field vary with sequence-stratigraphic position, although the relationship is qualitative rather than statistically tested. Relative sea-level shifts drive sediment deposition and reservoir architecture, and the three sequence boundaries SB1 through SB3 define two complete depositional cycles. Each cycle contains Lowstand, Transgressive, and Highstand system tracts, with Maximum Flooding Surfaces marking maximum marine influence. Lowstand tracts in the field generally contain some of the more favourable reservoir intervals. Sediment supply increases basinward during these phases, and clean, sand-rich, laterally continuous bodies are deposited. LST sandstones are commonly thicker and less shaly, with favourable static storage and log-derived flow characteristics relative to many transgressive intervals. During transgression, retrogradational stacking introduces more shale, and the Maximum Flooding Surface is usually the shaliest interval in the cycle, making it a useful seal. Highstand deposits can still host reservoir-quality sands where progradation and coarsening-upward trends develop.

This explains why LST-associated reservoirs across the BX Field are more favourable: they consist mostly of clean, sand-rich deposits formed under high-energy, progradational conditions. The predominance of these sandstone units, together with their relatively low shale content, enhances both storage and fluid-flow capacity. This is demonstrated by the BX-R0 reservoir, particularly in BX-05, where porosity and permeability reach 33.83% and 19.96 D, respectively. However, porosity and permeability vary considerably among wells because of differences in sand–shale distribution, depositional facies, and pore connectivity. The wide permeability range illustrates that high porosity does not necessarily imply high flow capacity where heterogeneity or shale content reduces pore connectivity. Because no core-permeability data were available, these empirical permeability estimates are interpreted comparatively rather than as direct predictions of well deliverability. Thus, intervals with comparable porosity may display substantially different permeability where variations in facies, shale content, and reservoir heterogeneity affect pore connectivity.

In addition to sequence-stratigraphic architecture, the structural framework of the BX Field also plays a major role in reservoir performance. The major faults mapped across the BX Field divide it into distinct structural blocks, and fault intersections coincide with closures that may provide favourable trapping geometry. The same faults, however, can isolate compartments from one another, potentially influencing pressure behaviour and fluid distribution across the field, although hydraulic isolation cannot be confirmed without dynamic data. These observations indicate that reservoir distribution and static quality in the BX Field reflect the combined influence of depositional facies and structural architecture. Therefore, understanding how depositional architecture, petrophysical variability, and structural geometry interact is essential for identifying productive compartments and positioning wells to improve recovery.

4. Conclusion

The present study provides an integrated understanding of reservoir quality in the BX Field as controlled by sequence-stratigraphic architecture, depositional facies, petrophysical variability, and structural configuration. Well-log data, seismic interpretation, and seismic–well ties were used to identify key stratigraphic surfaces, two complete depositional sequences, and Lowstand, Transgressive, and Highstand System Tracts. Mapped reflection terminations, onlap and downlap patterns, interpreted faults, structural highs, and closure geometry constrain depositional trends, reservoir distribution, and trapping style across the field. Petrophysical results show clear reservoir heterogeneity among the mapped intervals. The BX-R0 reservoir, which is predominantly developed within the Lowstand System Tracts, comprises sand-rich deposits that may be consistent with turbiditic deposition and generally exhibits favourable reservoir properties, including relatively high porosity, good permeability, low shale content, and a high net-to-gross ratio. These characteristics are particularly evident in wells BX-05 and BX-07, suggesting favourable storage and flow potential. BX-R0 in BX-04 further shows that favourable reservoir-rock properties do not necessarily imply hydrocarbon charge because this interval is water-dominated. In contrast, reservoir BX-R is relatively more shale-prone and heterogeneous, with comparatively lower porosity and permeability, and is mainly associated with Transgressive and Highstand System Tracts.

The available well-log and seismic evidence supports stratigraphic correlation of these intervals and suggests variations in reservoir continuity; however, hydraulic connectivity cannot be confirmed without dynamic pressure or production data. Overall, the results suggest that systems-tract position may influence reservoir quality in the BX Field, although the strength of this relationship remains subject to the limitations of the available data. Lowstand deposits are commonly associated with favourable reservoir characteristics, particularly where clean, sand-rich, progradational facies are developed. Highstand intervals may also contain good-quality reservoirs, whereas Transgressive intervals tend to be more shale-prone. These observations indicate a relationship between systems-tract position and reservoir quality, although its magnitude is not statistically quantified in the present study. Interpretation of reservoir distribution and hydrocarbon accumulation in the field therefore requires an integrated understanding of stratigraphy, depositional facies, structural configuration, and petrophysical properties. Overall, integrated sequence-stratigraphic and petrophysical evaluation provides a useful framework for predicting reservoir heterogeneity and hydrocarbon potential in the deep-offshore Niger Delta, with practical applications in reservoir modelling, well placement, appraisal planning, and development strategy in complex deep-water depositional systems.

Limitation of the study

The absence of core and biostratigraphic data limited validation of lithofacies, petrophysical estimates, and chronostratigraphic interpretations, making the sequence-stratigraphic framework partly interpretive. In addition, checkshot data were available for only one well, introducing greater uncertainty into the time–depth relationship and horizon-depth conversion; this limitation is acknowledged in the interpretation. Permeability is based on an empirical porosity–Swirr correlation rather than core measurements, while saturation estimates depend on the adopted electrical parameters and log-derived Rw and Rsh endpoints. These limitations should be considered when the static results are used for development decisions.

Data availability

The data supporting the findings of this study are available from the corresponding author upon reasonable request.

Declaration of competing interest

The authors declare that they have no known competing financial interests or personal relationships that could have appeared to influence the work reported in this manuscript.

Funding

The authors self-funded this research.

Acknowledgment

The authors acknowledge the Department of Geophysics, Federal University Oye-Ekiti, and the Nigerian Upstream Petroleum Regulatory Commission for providing the data used in this research.

References

[1] A. O. Fajana, "3-D static modelling of lateral heterogeneity using geostatistics and artificial neural network in reservoir characterisation of 'P' field, Niger Delta", NRIAG Journal of Astronomy and Geophysics **9** (2020) 129. https://doi.org/10.1080/20909977.2020.1727674.

[2] S. Rajput & R. K. Pathak, *Reservoir delineation and characterization*, in *Seismic exploration to reservoir excellence*, Springer, Singapore, 2025, pp. 321–394. https://doi.org/10.1007/978-981-96-1293-2_7.

[3] A. O. Fajana, A. M. Olawale & H. A. Oyesomi, "Quantitative reservoir evaluation and hydrocarbon volumetrics: An integrated petrophysical and 3-D static modeling approach in 'Hamphidex' field, Niger Delta, Nigeria", Journal of the Nigerian Society of Physical Sciences **7** (2025) 2429. https://doi.org/10.46481/jnsps.2025.2429.

[4] R. Alamu & O. J. Dada, "Sedimentary basins and hydrocarbon accumulation", ResearchGate (2025). https://www.researchgate.net/publication/390349023.

[5] O. Catuneanu, "Scale in sequence stratigraphy", Marine and Petroleum Geology **106** (2019) 128. https://doi.org/10.1016/j.marpetgeo.2019.04.026.

[6] A. O. Fajana, "Hydrocarbon reservoir characterization methodologies and uncertainties as a function of spatial location: A review from gigascale to nanoscale", FUOYE Journal of Pure and Applied Sciences **8** (2023) 82. https://fjpas.fuoye.edu.ng/index.php/fjpas/article/view/276.

[7] J. Ajidahun, O. A. Oluwajana, O. A. Olatunji & Y. O. Odusanwo, "Evaluation of geomechanical properties for CO_2 sequestration in an offshore field, Niger Delta Basin, Nigeria", Journal of Earth System Science **135** (2026) 31. https://doi.org/10.1007/s12040-026-02740-4.

[8] A. O. Fajana, M. A. Ayuk, P. A. Enikanselu & A. R. Oyebamiji, "Seismic interpretation and petrophysical analysis for hydrocarbon resource evaluation of 'Pennay' field, Niger Delta", Journal of Petroleum Exploration and Production Technology **9** (2019) 1025. https://doi.org/10.1007/s13202-018-0579-4.

[9] C. F. Ejeke, E. E. Anakwuba, I. T. Preye, O. G. Kakayor & I. E. Uyouko, "Evaluation of reservoir compartmentalization and property trends using static modelling and sequence stratigraphy", Journal of Petroleum Exploration and Production Technology **7** (2017) 361. https://doi.org/10.1007/s13202-016-0285-z.

[10] A. O. Fajana, M. A. Ayuk & P. A. Enikanselu, "Application of multilayer perceptron neural network and seismic multiattribute transforms in reservoir characterization of Pennay field, Niger Delta", Journal of Petroleum Exploration and Production Technology **9** (2019) 31. https://doi.org/10.1007/s13202-018-0485-9.

[11] A. O. Owoyemi, *Sequence stratigraphy of Niger Delta, Delta field, offshore Nigeria, M.S. thesis*, Texas A&M University, College Station, TX, USA, 2004. https://hdl.handle.net/1969.1/2768.

[12] P. S. Ola, J. O. Aghomon & A. O. Alabere, "Sequence stratigraphy and petrophysical analysis of 'Aje' field, offshore Niger Delta", Journal of Scientific and Engineering Research **8** (2021) 167. https://doi.org/10.5281/zenodo.10589294.

[13] K. A. Haruna, J. K. Raji, A. Y. Jimoh, J. A. Adeoye, O. O. Alu, A. A. Badmus & B. Garba, "Biostratigraphy and paleoenvironment studies of shales from Owan-1 well, Niger Delta Basin, Nigeria", Journal of the Nigerian Society of Physical Sciences **7** (2025) 2183. https://doi.org/10.46481/jnsps.2025.2183.

[14] B. A. Olisa & A. O. Edjere, "Integration of sequence stratigraphy and petrophysical analysis for reservoir characterization: A case study of 'ED' field, offshore Niger Delta", Journal of Environment and Earth Science **13** (2023) 49. https://doi.org/10.7176/JEES/13-1-05.

[15] A. O. Fajana, M. A. Ayuk & T. D. Omoyegun, "Comparison of modified Waxman–Smith algorithms and Archie models in prospectivity analysis of saturations in shaly-sand reservoirs: A case study of Pennay field, Niger Delta", Earth Science Informatics **14** (2021) 1647. https://doi.org/10.1007/s12145-021-00592-8.

[16] F. M. El-Fawal, M. A. Sarhan, R. E. Ll. Collier, A. Basal & M. H. Abdel Aal, "Sequence stratigraphic evolution of the post-rift megasequence in the northern part of the Nile Delta Basin, Egypt", Arabian Journal of Geosciences **9** (2016) 585. https://doi.org/10.1007/s12517-016-2602-8.

[17] B. D. Evamy, J. Haremboure, P. Kamerling, W. A. Knaap, F. A. Molloy & P. H. Rowlands, "Hydrocarbon habitat of Tertiary Niger Delta", AAPG Bulletin **62** (1978) 1. https://doi.org/10.1306/C1EA47ED-16C9-11D7-8645000102C1865D.

[18] H. Doust & E. Omatsola, *Niger Delta*, in *Divergent/passive margin basins*, J. D. Edwards & P. A. Santogrossi (Eds.), AAPG Memoir 48, American Association of Petroleum Geologists, Tulsa, OK, USA, 1990, pp. 239–248. https://doi.org/10.1306/M48508C4.

[19] J. Ajidahun, O. A. Oluwajana, O. Olabode & O. A. Olatunji, "Development of operational CO_2 injection guidelines through integrated geomechanical and reservoir simulation: A case study from the Niger Delta Basin, Nigeria", Journal of African Earth Sciences **239** (2026) 106126. https://doi.org/10.1016/j.jafrearsci.2026.106126.

[20] F. Corredor, J. H. Shaw & F. Bilotti, "Structural styles in the deep-water fold and thrust belts of the Niger Delta", AAPG Bulletin **89** (2005) 753. https://doi.org/10.1306/02170504074.

[21] P. M. Shannon & D. Naylor, *Petroleum basin studies*, Graham & Trotman, London, UK, 1989.

[22] J. E. Ejedawe, S. J. L. Coker, D. O. Lambert-Aikhionbare, K. B. Alofe & F. O. Adoh, "Evolution of oil-generative window and oil and gas occurrence in Tertiary Niger Delta Basin", AAPG Bulletin **68** (1984) 1744. https://doi.org/10.1306/AD46198F-16F7-11D7-8645000102C1865D.

[23] C. C. Ugbor, C. I. Ugwuoke & P. O. Odong, "Hydrocarbon prospectivity and risk assessment of 'Bob' field Central Swamp Depobelt, onshore Niger Delta Basin, Nigeria", Open Journal of Geology **13** (2023) 847. https://doi.org/10.4236/ojg.2023.138038.

[24] J. Ajidahun, O. A. Oluwajana, A. S. Ifanegan & Y. O. Odusanwo, "Structural and petrophysical assessment of CO_2 storage in depleted Z-field reservoirs, offshore Niger Delta Basin", Marine Georesources & Geotechnology **44** (2026) 330. https://doi.org/10.1080/1064119X.2025.2498030.

[25] A. O. Fajana, A. M. Olawale, A. B. Eluwole, H. A. Oyesanmi & T. S. Fagbemigun, "Petrophysical parameters analysis and formation evaluation for hydrocarbon resources in 'Hamdex' field, offshore Niger Delta", FUTA Journal of Sustainable Technology **13** (2024) 73. https://journals.futa.edu.ng/home/paperd/1544/96.

[26] V. V. Larionov, *Radiometry of boreholes*, Nedra, Moscow, USSR, 1969.

[27] G. E. Archie, "The electrical resistivity log as an aid in determining some reservoir characteristics", Petroleum Transactions of AIME **146** (1942) 54. https://doi.org/10.2118/942054-G.

[28] A. O. Fajana, "Hydrocarbon reservoir characterization using multipoint stochastic inversion technique: A case study of Pennay field", Natural Resources Research **30** (2021) 1305. https://doi.org/10.1007/s11053-020-09762-9.

[29] T. S. Fagbemigun, A. O. Fajana, O. D. Odebunmi, O. E. Oyanameh, J. Tsado & W. O. Osisanya, "Petrophysical parameters analysis and reservoir evaluation of 'ATINUK' field, offshore Niger Delta Basin", Savanna Journal of Basic and Applied Sciences **6** (2024) 74. https://doi.org/10.59298/sjbas/2024/6.1.7485.

[30] D. O. Anomneze, A. U. Okoro, N. E. Ajaegwu, E. O. Akpunonu, C. V. Ahaneku, T. A. D. Ede, G. C. Okeugo & C. F. Ejeke, "Application of seismic stratigraphy and structural analysis in the determination of petroleum plays within the Eastern Niger Delta Basin, Nigeria", Journal of Petroleum Exploration and Production Technology **5** (2015) 113.

https://doi.org/10.1007/s13202-015-0161-2.
[31] A. O. Fajana, "Analytical modelling of fault seal effectiveness in hydrocarbon reservoirs: A multi-criteria decision analysis and analytical hierarchy process approach", ABUAD International Journal of Natural and Applied Sciences **4** (2025) 103. https://doi.org/10.53982/aijnas.2024.0402.15-j.